Journal of Sound and Vibration 329 (2010) 5249–5272

Contents lists available at ScienceDirect

Journal of Sound and Vibration

journal homepage: www.elsevier.com/locate/jsvi

Indirect measurement of dynamic force transmitted by a nonlinear hydraulic mount under sinusoidal excitation with focus on super-harmonics

Jong-Yun Yoon, Rajendra Singh *

Acoustics and Dynamics Laboratory, Smart Vehicle Concepts Center, Department of Mechanical Engineering, The Ohio State University, Columbus, OH 43210, USA

ARTICLE INFO

Article history:
Received 3 May 2010
Received in revised form
29 June 2010
Accepted 30 June 2010
Handling Editor: H. Ouyang
Available online 29 July 2010

ABSTRACT

Direct measurement of forces is not practical in many real-life applications since the interfacial conditions may change. Thus indirect force estimation methods must be developed though they pose special difficulty for nonlinear mounts or isolators. The hydraulic engine mount is examined as an illustrative example in this article since it exhibits spectrally varying and amplitude-sensitive parameters. First, we propose linear time-invariant, nonlinear and quasi-linear fluid and mechanical system models. Second, models are utilized to predict the transmitted force time history under sinusoidal excitation conditions given measured (or calculated) motion and/or internal pressure time histories. Experimental data from the non-resonant dynamic stiffness test is investigated in both time and frequency domains. In particular, the super-harmonic contents in fluid chamber pressure and force time histories are investigated using both measurements and mathematical models. This paper examines several alternate indirect schemes for estimating dynamic forces and highlights their strengths. The quasi-linear model with effective system parameters, say in terms of force to pressure or force to motion transfer functions, is found to correlate well with measured dynamic forces though linear and nonlinear models could be employed as well.

1. Introduction

Precise knowledge of the dynamic forces that are transmitted by machinery mounts and isolators to rigid or compliant bases in vehicles, buildings, and equipment is critical to the dynamic design and vibration control considerations. Direct measurement of forces (for example, using conventional force transducers) is not practical in many real-life applications since the interfacial conditions may change [1,2]. Thus indirect force estimation methods must be developed [3,4]. For instance, one could employ transfer path approaches, though they are applicable primarily in the frequency domain for a linear time-invariant system [5,6]. Also, dynamic forces could be estimated by using other measured signals such as operating motions, but then dynamic stiffness must be known a priori [7]. Such indirect force estimation methods pose special difficulty for nonlinear mounts or isolators. For instance, hydraulic engine mounts exhibit spectrally varying and amplitude-sensitive parameters [8].

To illustrate the concepts of this article, consider Fig. 1(a) that displays the internal configuration of the hydraulic engine mount and its fluid system model; it will be discussed further in Section 3. Fig. 1(b) shows the non-resonant dynamic stiffness test concept, as defined by the ISO standard 10846 [9]. Here, f_m is the preload, $x(t) = x_m + \mathrm{Re}[\tilde{X}\, e^{i\omega_o t}]$ is the excitation displacement, x_m is the mean displacement, $\tilde{X} = X e^{i\varphi_X}$ is the complex valued excitation amplitude, X is

* Corresponding author. Tel.: +1 614 292 9044; fax: +1 614 292 3163.
E-mail address: singh.3@osu.edu (R. Singh).

0022-460X/$ - see front matter © 2010 Elsevier Ltd. All rights reserved.
doi:10.1016/j.jsv.2010.06.026

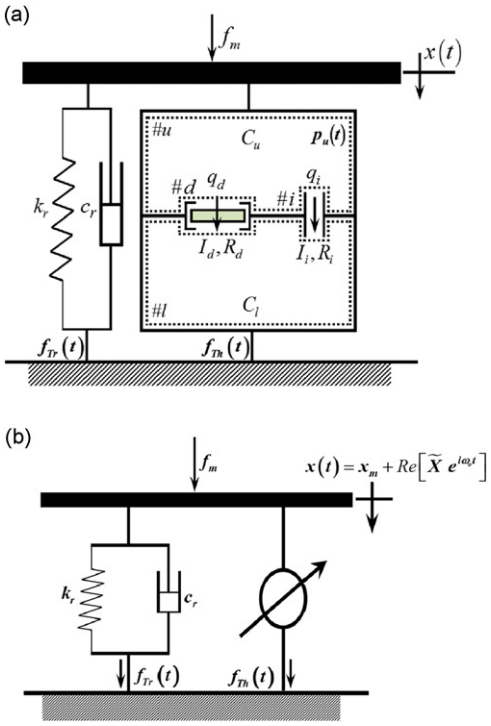

Fig. 1. Force transmitted $f_T(t)$ by a hydraulic mount in the context of non-resonant elastomeric test [1]: (a) fluid model of the hydraulic mount and its parameters for rubber and hydraulic paths and (b) sinusoidal displacement excitation $x(t)$ and dynamic forces transmitted by two paths (f_{Tr} and f_{Th}).

the amplitude of displacement, φ_X is the phase of $x(t)$, ω_o is the excitation (fundamental) frequency (rad s^{-1}), and Re[] is the real value operator; tilde over a symbol implies that is complex valued. In addition, a pressure transducer, $p_u(t)$, is also installed in the upper chamber in our laboratory experiments. As shown in Fig. 1(b), the steady state force transmitted $f_T(t)$, in time (t) domain, is related to the excitation displacement $x(t)$ and upper chamber response $p_u(t)$:

$$f_T(t) = f_{Tr}(t) + f_{Th}(t), \tag{1}$$

$$f_{Tr}(t) = c_r\dot{x}(t) + k_r x(t), \tag{2}$$

$$f_{Th}(t) = A_r p_u(t). \tag{3}$$

Here, $f_{Tr}(t)$ is the rubber path force (subscript r), $f_{Th}(t)$ is the hydraulic path force (subscript h), k_r and c_r are the rubber stiffness and damping coefficient, respectively, and A_r is the effective piston area. Our experiments show that $p_u(t)$ deviates from the sinusoidal shape depending on X and ω_o, as discussed later in the paper. Likewise, k_r and c_r vary as well with X and ω_o. The chief goal of this article is, therefore, to propose linear time-invariant (LTI), nonlinear (NL), and quasi-linear (QL) models that could be utilized to predict the force time history under sinusoidal excitation conditions given measured (or calculated) motion and/or internal pressure time histories. In particular, the super-harmonic contents in $p_u(t)$ and $f_T(t)$ time histories are investigated using both measurements and mathematical models. Even though the focus of this article is on hydraulic engine mounts, its concepts could be extended to real-life system problems [1,5,6]. For instance, we are estimating forces in a nonlinear isolation system using a dynamic load sensing device.

2. Initial results and objectives

Fig. 2 presents the initial results based upon Eqs. (1) to (3) when only the fundamental measured (designated with subscript M) $x_M(t)$ and $p_{uM}(t)$ signal terms (as shown in Fig. 2(a)) are considered. At this juncture, the following nominal (and constant) parameters are incorporated in Eqs. (1) to (3): $k_r = 2\times10^5$ N m^{-1}; c_r=496.1 N-s m^{-1}; $A_r = 4\times10^{-3}$ m^2. This formulation is designated as a 'simple prediction model', and its results are compared in Fig. 2(b) with the direct measurements of dynamic force; both single term and multi-term time histories are displayed. The results show the same order of magnitudes, but the precise time history deviates from the sinusoidal shape. This suggests that super-harmonic terms must be included in $p_u(t)$. Also, a better knowledge of the amplitude (X) and frequency sensitive parameters is needed.

Fluid and mechanical system models of hydraulic engine mounts, based on the linear time-invariant system theory, have been extensively investigated for both fixed and free decoupler mounts [2,10,11]. Nevertheless, their dynamic

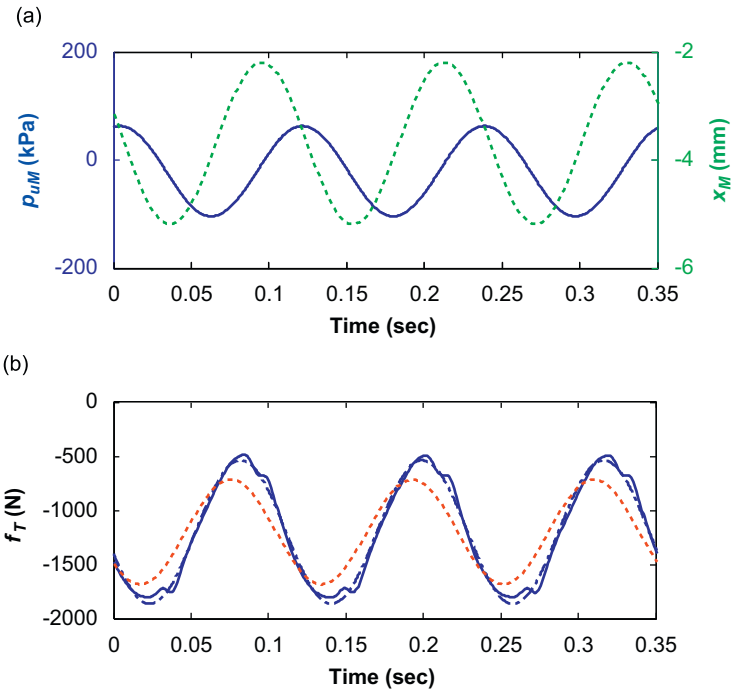

Fig. 2. Measurement of upper chamber pressure and transmitted force time histories for the free decoupler mount, given sinusoidal displacement $x(t) = \mathrm{Re}[\tilde{X}\, e^{i\omega_o t}]$ at $\omega_o/2\pi$=8.5 Hz and X=1.5 mm: (a) $x_M(t)$ with X=1.5 mm and $p_{uM}(t)$ time histories with single harmonic term; Key for part (a): ·····, $x_M(t)$; ——, $p_{uM}(t)$ with a single harmonic term; (b) measured and predicted forces, $f_T(t)$; Key for part (b); ——, measured force with many harmonics; ·····, measured force with a single harmonic term; ·····, predicted force with nominal parameters and a single harmonic term.

characteristics depend upon the amplitude and frequency of excitation [12]. Thus, nonlinear models have been suggested under both steady state and transient conditions [13–20]. For instance, He and Singh [18] developed the discontinuous nonlinear model when the hydraulic mount is excited by a step-up or step-down input. Lee and Singh [19,20] have found that the nonlinear responses (of a quarter vehicle model with hydraulic mount) are affected by the super-harmonic terms even though the system is excited by a pure sinusoidal force. Unlike prior articles [15–18] that describe various mount models, this paper focuses on the prediction of dynamic forces by using alternate methods.

The scope of this article is limited to the mount only, and steady state experiments under sinusoidal excitation from 1 to 50 Hz with X from 0.15 to 1.5 mm (zero-to-peak) are considered. In all cases, $x_M(t)$, $p_{uM}(t)$, and $f_{TM}(t)$ are measured on the elastomer test machine for both fixed and free decoupler mounts. Specific objectives are as follows: (1) analyze the measured $p_{uM}(t)$ and $f_{TM}(t)$ in both time and frequency domains and examine their spectral contents; (2) develop linear time-invariant and nonlinear models of both fixed and free decoupler mounts and compare their $f_T(t)$ predictions with measurements; (3) propose a quasi-linear model with spectrally varying and amplitude-sensitive parameters at both ω_o and $n\omega_o$ (n=2, 3, 4, …) terms; both fluid and analogous mechanical system models are used to predict $f_T(t)$ and compare with $f_{TM}(t)$; and (4) estimate $f_T(t)$ in the time domain by using the Fourier series expansion.

3. Linear time-invariant (LTI) model for fluid system

First, we develop the linear time-invariant (LTI) model for the fluid system of Fig. 1(a) with the following assumptions: (1) the hydraulic mount is excited by a pure sinusoidal displacement $x(t)$ under a mean load f_m, and it reaches steady state and (2) the hydraulic mount is attached to a rigid base. The momentum and continuity equations for the hydraulic path are as follows [10–16]:

$$f_T(t) = c_r\dot{x}(t) + k_r x(t) + A_r p_u(t), \tag{4}$$

$$p_u(t) - p_l(t) = I_i\dot{q}_i(t) + R_i q_i(t), \tag{5}$$

$$p_u(t) - p_l(t) = I_d\dot{q}_d(t) + R_d q_d(t), \tag{6}$$

$$C_u\dot{p}_u(t) = A_r\dot{x}(t) - q_i(t) - q_d(t), \tag{7}$$

$$C_l\dot{p}_l(t) = q_i(t) + q_d(t). \tag{8}$$

Here, C_u and C_l are the upper (#u) and lower (#l) chamber compliances, respectively; I_i and I_d are the inertances of the inertia track (#i) and decoupler (#d), respectively; R_i and R_d are the resistances of the inertia track and decoupler, respectively; and q_i and q_d are the fluid flow through inertia track and decoupler, respectively. Transform Eqs. (4)–(8) into the Laplace domain (s) with the assumption that the initial conditions are zeros

$$F_T(s) = (c_r s + k_r)X(s) + A_r P_u(s), \tag{9}$$

$$P_u(s) - P_l(s) = (I_i s + R_i)Q_i(s), \tag{10}$$

$$P_u(s) - P_l(s) = (I_d s + R_d)Q_d(s), \tag{11}$$

$$C_u s P_u(s) = A_r s X(s) - Q_i(s) - Q_d(s), \tag{12}$$

$$C_l s P_l(s) = Q_i(s) + Q_d(s). \tag{13}$$

To facililate models and experimental estimations, we define dimensionless variables and parameters as: $\overline{X} = X/X_{\text{ref}}$ = the dimensionless excitation displacement amplitude; X_{ref}=reference displacement amplitude; $\overline{P}_u = P_u/P_{\text{uref}}$ =dimensionless pressure; P_{uref}=($k_{\text{rref}}X_{\text{ref}}$)/$A_r$=reference pressure; k_{rref}=reference stiffness; $\overline{F}_T = F_T/F_{T\text{ref}}$ =dimensionless force; and $F_{T\text{ref}}$=$k_{\text{rref}}X_{\text{ref}}$=reference force. We now define three dimensionless transfer functions that relate $\overline{F}_T$ to $\overline{P}_u$ and $\overline{X}$

$$\overline{G}(s) = \frac{\overline{P}_u}{\overline{X}}(s) = \frac{A_r}{k_{\text{rref}}}\frac{P_u}{X}(s) = \gamma_h \left(\frac{s^2}{\omega_{N1}^2} + \frac{2\zeta_1}{\omega_{N1}}s + 1\right) \Big/ \left(\frac{s^2}{\omega_{N2}^2} + \frac{2\zeta_2}{\omega_{N2}}s + 1\right), \tag{14}$$

$$\overline{K}(s) = \frac{\overline{F}_T}{\overline{X}}(s) = \frac{1}{k_{\text{rref}}}\frac{F_T}{X}(s), \tag{15}$$

$$\overline{H}(s) = \frac{\overline{F}_T}{\overline{P}_u}(s). \tag{16}$$

Here, $\overline{G}(s)$ is the dimensionless pressure to displacement transfer function, $\overline{K}(s)$ is the dimensionless cross point dynamic stiffness, and $\overline{H}(s)$ is the dimemsionless force transmissibility. Using Eqs. (9)–(16), the above transfer functions are expressed in terms of natural frequencies (ω_{N1} and ω_{N2}), damping ratios (ζ_1 and ζ_2), and hydraulic path static stiffness γ_h as expressed below for both fixed and free decoupler mounts; these system parameters are derived in our earlier paper [2]

$$\omega_{N1(\text{fixed})} = \sqrt{\frac{1}{C_l I_i}}, \tag{17}$$

$$\omega_{N1(\text{free})} = \sqrt{\frac{R_i + R_d}{C_l I_i R_d}}, \tag{18}$$

$$\omega_{N2(\text{fixed})} = \sqrt{\frac{C_u + C_l}{C_u C_l I_i}}, \tag{19}$$

$$\omega_{N2(\text{free})} = \sqrt{\frac{(C_u + C_l)(R_i + R_d)}{C_u C_l I_i R_d}}, \tag{20}$$

$$\zeta_{1(\text{fixed})} = \frac{1}{2}\sqrt{\frac{C_l R_i^2}{I_i}}, \tag{21}$$

$$\zeta_{1(\text{free})} = \frac{1}{2}\left(\sqrt{\frac{C_l R_d R_i^2}{I_i(R_i + R_d)}} + \sqrt{\frac{I_i}{C_l R_d (R_i + R_d)}}\right), \tag{22}$$

$$\zeta_{2(\text{fixed})} = \frac{1}{2}\sqrt{\frac{C_u C_l R_i^2}{I_i(C_u + C_l)}}, \tag{23}$$

$$\zeta_{2(\text{free})} = \frac{1}{2}\left[\sqrt{\frac{C_u C_l R_d R_i^2}{I_i(C_u + C_l)(R_i + R_d)}} + \sqrt{\frac{(C_u + C_l)I_i}{C_u C_l R_d (R_i + R_d)}}\right], \tag{24}$$

$$\gamma_h = \frac{A_r^2}{k_{\text{rref}}(C_u + C_l)}. \tag{25}$$

Here, subscripts (fixed) and (free) refer to the fixed and free decoupler mount designs, respectively. Next, decompose the dynamic stiffness into rubber (subscript r) and hydraulic (subscript h) paths as

$$\overline{K}(s)=\overline{K}_r(s)+\overline{K}_h(s), \tag{26}$$

$$\overline{K}_r(s)=\frac{\overline{F}_{Tr}}{\overline{X}}(s)=\gamma_r(1+\tau_r s), \tag{27}$$

$$\overline{K}_h(s)=\frac{\overline{F}_{Th}}{\overline{X}}(s)=\gamma_h\left(\frac{s^2}{\omega_{N1}^2}+\frac{2\zeta_1}{\omega_{N1}}s+1\right)\Big/\left(\frac{s^2}{\omega_{N2}^2}+\frac{2\zeta_2}{\omega_{N2}}s+1\right), \tag{28}$$

Finally, decompose the force transmissibility as well:

$$\overline{H}(s)=\overline{H}_r(s)+\overline{H}_h(s), \tag{29}$$

$$\overline{H}_r(s)=\frac{\overline{F}_{Tr}}{\overline{P}_u}(s)=\frac{\gamma_r}{\gamma_h}(1+\tau_r s)\left(\frac{s^2}{\omega_{N2}^2}+\frac{2\zeta_2}{\omega_{N2}}s+1\right)\Big/\left(\frac{s^2}{\omega_{N1}^2}+\frac{2\zeta_1}{\omega_{N1}}s+1\right), \tag{30}$$

$$\overline{H}_h(s)=\frac{\overline{F}_{Th}}{\overline{P}_u}(s)=1, \tag{31}$$

$$\tau_r=\frac{c_r}{k_r}, \tag{32}$$

$$\gamma_r=\frac{k_r}{k_{rref}}. \tag{33}$$

Here, τ_r is the time constant and γ_r is the rubber path static stiffness. Observe that the fixed decoupler case is derived from the free decoupler formulations by assuming that $I_d=0$ and $R_d\to\infty$. In our study, the nominal parameters are as follows: $I_i=4\times10^6$ kg m^{-4}; $I_d=509.3$ kg m^{-4}; $C_u=2.5\times10^{-11}$ m^5 N^{-1}; $C_l=2.4\times10^{-9}$ m^5 N^{-1}; $R_i=2\times10^8$ N s m^{-5}; $R_d=5\times10^8$ N s m^{-5}. Reference values are selected as: $k_{rref}=2.0\times10^5$ N m^{-1}, $A_r=4.5\times10^{-3}$ m^2; and $X_{ref}(\times10^{-3}$ m) though different values of X_{ref} according to the experimental excitation amplitudes are utilized.

4. Linear time-invariant (LTI) model for analogous mechanical system

Fig. 3 illustrates the analogous mechanical system LTI model with effective parameters that could be related to the fluid system properities. The governing equations are

$$m_{ie}\ddot{x}_{ie}(t)+c_{ie}\dot{x}_{ie}(t)+(k_u+k_l)x_{ie}(t)=k_u x(t), \tag{34}$$

$$f_T(t)=c_r\dot{x}(t)+k_r x(t)+k_l x_{ie}(t). \tag{35}$$

Here, the mechanical parameters are defined as follows: effective mass of inertia track fluid column $m_{ie}=A_r^2 I_i$; effective viscous damping of inertia track fluid $c_{ie}=A_r^2 R_i$; equivalent stiffness of upper chamber compliance $k_u=A_r^2/C_u$; and equivalent stiffness of lower chamber compliance $k_l=A_r^2/C_l$; and effective velocity of inertia track fluid $\dot{x}_{ie}(t)=q_i(t)/A_r$. By transforming Eqs. (34) and (35) into the Laplace domain (s) and ignoring initial conditions, the dimensionless transfer functions, like the

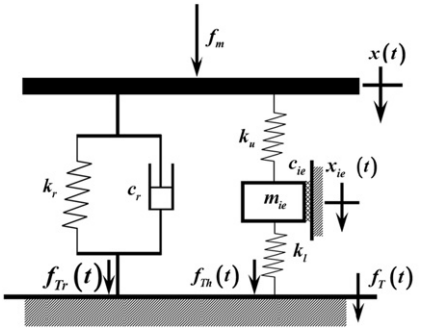

Fig. 3. Analogous mechanical system model and its parameters for rubber and hydraulic paths.

fluid system model, are derived:

$$\frac{\overline{F}_T}{\overline{X}}(s)=\overline{K}_A(s)=\frac{\overline{F}_{Ar}}{\overline{X}}(s)+\frac{\overline{F}_{Ah}}{\overline{X}}(s)=\overline{K}_{Ar}(s)+\overline{K}_{Ah}(s), \tag{36}$$

$$\overline{K}_{Ar}(s)=\gamma_r(1+\tau_r s), \tag{37}$$

$$\overline{K}_{Ah}(s)=\gamma_h\Big/\left(\frac{s^2}{\omega_{N2}^2}+\frac{2\zeta_2}{\omega_{N2}}s+1\right). \tag{38}$$

Here, $\overline{K}_A(s)$ indicates the dimensionless dynamic stiffness (with subscript A) of the analogous mechanical system. The values of nominal parameters are: m_{ie}=81 kg; $c_{ie}=4.1\times10^3$ N s m^{-1}; $k_u=8.1\times10^5$ N m^{-1}; $k_l=8.4\times10^3$ N m^{-1}. Our study will focus on $\overline{K}(s)$ and $\overline{H}(s)$ from the fluid system model as described by Eqs. (15)–(33), and $\overline{K}_A(s)$ from the analogous mechanical system model as given by Eqs. (36)–(38).

5. Nonlinear (NL) model for fluid system

The differntial equations for the fluid system as given in Eqs. (4) to (8) are now modified to include four nonlinearities [15,16]. The sign convention is as follows: $p_u(t)$ is positive (in compression) corresponding to the upward (positive) motion of $x(t)$, $q_i(t)$; and $q_d(t)$; and $p_u(t)$ is negative (in expansion) for the downward motion of $x(t)$, $q_i(t)$ and $q_d(t)$; $f_T(t)$ follows the $x(t)$ sign. First we express the governing equations in the state space form where the state variable is defined as $\underline{S}(t)=[p_1(t)p_2(t)q_i(t)\dot{x}_d(t)f_T(t)]^T$; here $\dot{x}_d(t)=\mathrm{q}_d(t)/A_d$, and A_d is the effective piston area of decoupler element

$$\dot{\underline{S}}(t)=\underline{\underline{B}}\,\underline{S}(t)+\underline{D}(t), \tag{39}$$

$$\underline{\underline{B}}=\begin{bmatrix}0 & 0 & 1/C_u & A_d/C_u & 0\\ 0 & 0 & -1/C_l & -A_d/C_l & 0\\ -1/I_i & 1/I_i & -R_i/I_i & 0 & 0\\ -A_d/m_d & A_d/m_d & 0 & -c_d/m_d & 0\\ 0 & 0 & -A_r/C_u & -A_rA_d/C_u & 0\end{bmatrix}, \tag{40}$$

$$\underline{D}(t)=\begin{bmatrix}-A_r\dot{x}(t)/C_u\\ 0\\ 0\\ 0\\ (A_r^2/C_u+k_r)\dot{x}(t)+c_r\ddot{x}(t)\end{bmatrix}. \tag{41}$$

where $\dot{x}(t)$ and $\ddot{x}(t)$ are the excitation velocity and acceleration, respectively; the effective mass of decoupler element is $m_d=A_d^2I_d$, and effecitve viscous damping of decoupler fluid is $c_d=A_d^2R_d$. The nominal parameters are: $m_d=6.0\times10^{-3}$ kg; c_d=100 N s m^{-1}; $A_d=1.96\times10^{-3}$ m^2.

The discontinuous motion of the decoupler element is given in terms of the switching mechanism as follows:

$$\ddot{x}_d(t)=\begin{cases}\dfrac{1}{m_d}[A_d\{-p_u(t)+p_l(t)\}-c_dx_d(t)], & -\dfrac{\delta_d}{2}<x_d(t)<\dfrac{\delta_d}{2},\\ 0, & \dot{x}(t)=0,\quad x_d(t)=-\dfrac{\delta_d}{2}\ \text{or}\ x_d(t)=\dfrac{\delta_d}{2},\end{cases} \tag{42}$$

where $x_d(t)$ and δ_d are the displcement of decoupler element and the net decoupler gap, respectively. The nonlinear functions for $C_u(p_u(t))$, $C_l(p_l(t))$, and $R_i(q_i(t))$ are described below based on prior work [15,16]

$$C_u(p_u(t))=a_0 \text{ when } p_u(t)\geq p_a, \tag{43}$$

$$C_u(p_u(t))=a_{17}[p_u(t)]^7+a_{10} \text{ when } p_1(t)<p_a, \tag{44}$$

$$C_l(p_l(t))=a_{23}[p_l(t)]^3+a_{22}[p_l(t)]^2+a_{21}p_l(t)+a_{20}, \tag{45}$$

$$R_i(q_i(t))=a_R|q_i(t)|. \tag{46}$$

Typical coefficients of $C_u(p_u(t))$, $C_l(p_l(t))$ and $R_i(q_i(t))$ are as follows under f_m=1200 N: $a_0=1.09\times10^{-11}$; $a_{17}=-7\times10^{-45}$; $a_{10}=2.5\times10^{-11}$, $a_{23}=1.51\times10^{-18}$; $a_{22}=-6.82\times10^{-14}$; $a_{21}=3.13\times10^{-9}$; $a_{20}=5.19\times10^{-6}$; $a_R=3.45\times10^{11}$. Further, the nonlinear model of the fixed decoupler mount is also examined with the assumptions that I_d=0 and $R_d\to\infty$ by essentially ignoring Eq. (42).

The nonlinear model is solved numerically using the Runge–Kutta integration technique. The initial values of $p_u(t)$ and $f_T(t)$ are selected from the measurements as follows: $x(0)=\mathrm{Re}[\tilde{X}]$; $\dot{x}(0)=\mathrm{Re}[i\omega_o\tilde{X}]$; and $f_T(0)=c_r\mathrm{Re}[i\omega_o\tilde{X}]+k_r\mathrm{Re}[\tilde{X}]+A_rp_u(0)$.

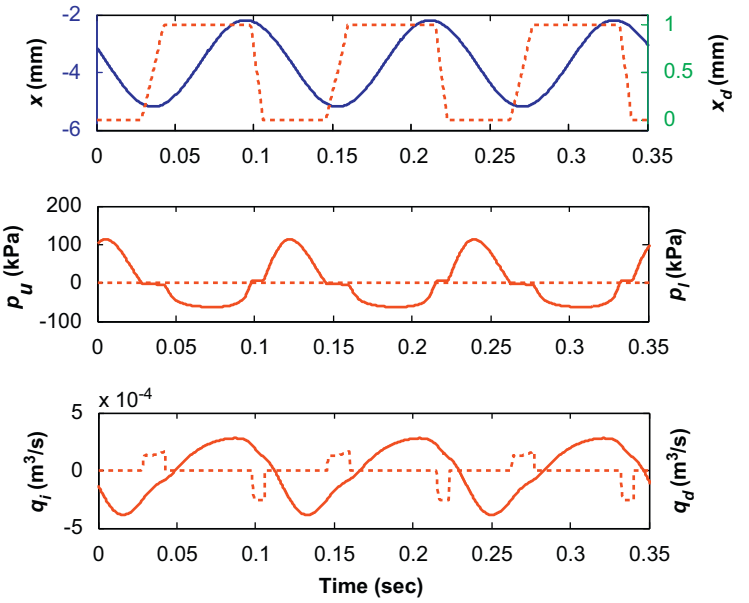

Fig. 4. Typical predictions of the nonlinear model for a free decoupler mount given sinusoidal exaction with X=1.5 mm and $\omega_o/2\pi$=8.5 Hz (observe the effect of the switching phenomena in pressure and flow rate time histories). Key: ——, $x_M(t)$; ——, $p_u(t)$ and $q_i(t)$; ·····, $x_d(t)$, $p_l(t)$ and $q_d(t)$.

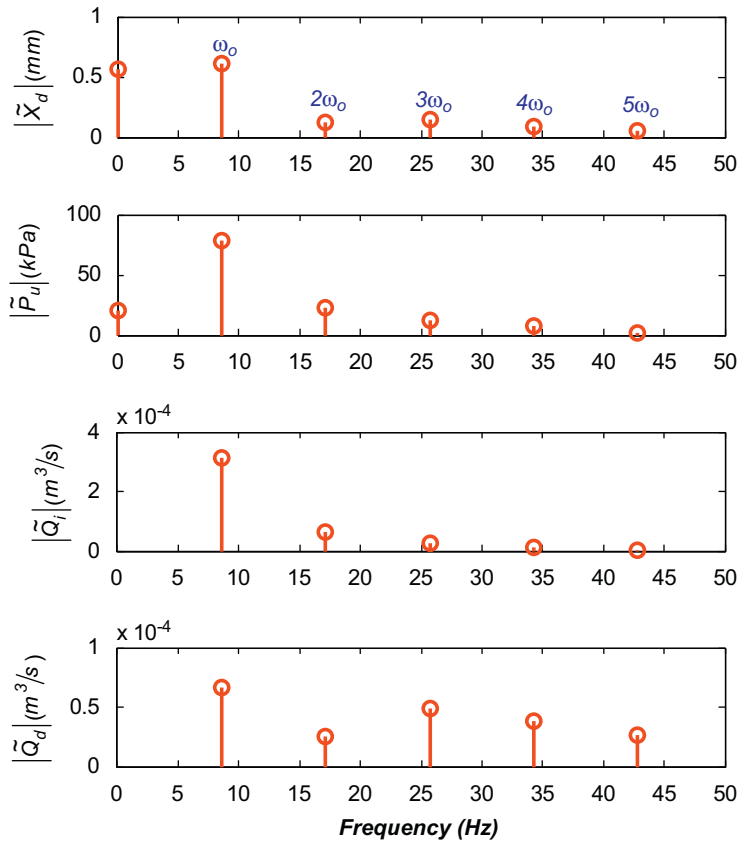

Fig. 5. Magnitude of $\tilde{X}_d$, $\tilde{P}_u$, $\tilde{Q}_i$ and $\tilde{Q}_d$ from the FFT analysis with a free decoupler mount by using the nonlinear model given sinusoidal excitation with X=1.5 mm and $\omega_o/2\pi$=8.5 Hz. Key: $\tilde{X}_d$, FFT of $x_d(t)$; $\tilde{P}_u$, FFT of $p_u(t)$; $\tilde{Q}_i$, FFT of $q_i(t)$; $\tilde{Q}_d$, FFT of $q_d(t)$.

The initial conditions of other states $p_l(t)$, $q_i(t)$, and $\dot{x}_d(t)$ are set to zeros. Here, the mean values x_m and f_m are assumed to be known. Thus, only the dynamic terms are considered. Figs. 4 and 5 show typical time histories and their Fourier magnitude spectra under sinusoidal excitation. The switching mechanism of the free decoupler is evident in pressure, decoupler motion and flow rate predictions. Also, the super-harmonic terms are clearly observed in $x_d(t)$, $p_u(t)$, $q_i(t)$ and $q_d(t)$ as shown in Fig. 5. The dynamic forces estimated by the nonlinear model including a comparison with measurements will be addressed later.

6. Quasi-linear (QL) model with effective parameters and super-harmonic terms

6.1. Spectrally varying and amplitude sensitive parameters

Next, we develop a quasi-linear (QL) model, say in terms of the transfer functions of Sections 3 and 4 that would include effective or empirical properties. Several issues must be considered since the hydraulic mount is a nonlinear device [13–17]. First, the causality problem must be considered as the measured signals are transferred into the frequency domain by using the fast Fourier transform (FFT) routine. This inherent problem could be understood by employing a Hilbert transform pair to represent the causal system in terms of the real and imaginary parts of a QL model [21–23]. Second, we assume that the upper chamber pressure is most affected by the nonlinear phenomena, and thus, all nonlinearities are lumped into the effective (subscript e) upper chamber compliance. The definition of C_{un} (static compliance under nominal conditions, with subscript n) has to be changed, and thus we define complex valued parameter $\widetilde{C}_{ue}(\omega,X)$ that includes both amplitude-sensitive stiffness and damping properties at any frequency. Relate static and dynamic compliances as: $\widetilde{C}_{ue}=\widetilde{\lambda}_u C_{un}=(\alpha+i\beta)C_{un}$, where $\widetilde{\lambda}_u(=\alpha+i\beta)$ is an empirical parameter whose coefficients α and β at any frequency would be determined from measurements. Similarly, the rubber path is formulated as disccused next. The overall quasi-linear model concept is shown in Fig. 6; it will be addressed further in Section 7.

6.2. Estimation of effective rubber force path parameters

To investigate the rubber force path, the anti-freeze mixture (water) is drained from the mount and then the mount is excited using the same method [7,9]. The spectrally varying and amplitude-sensitive parameters of the rubber path such as $k_{re}(\omega_o,X_1)$ and $c_{re}(\omega_o,X_1)$ are determined only at the fundamental frequency (ω_o) where the subscript e designates the effective value. Here X_1 is the 'virtual' excitation displacement amplitude at ω_o as shown in Table 1, which will be further explained in the next section. Fig. 7 shows sample $k_{re}(\omega_o,X_1)$ and $c_{re}(\omega_o,X_1)$ data with X=0.15 mm. In our study, the data set consists of 7 cases corresponding to X=0.15, 0.25, 0.5, 0.75, 1.0, 1.25, 1.5 mm. Therefore, the quasi-linear model with curve-fit functions can be developed given experimental data [2]. The goal is to develop continuous profiles of the quasi-linear parameters $\lambda_{kr}(\omega_o,X_1)$ as a function of frequency $\Omega(=\omega_o/2\pi$, Hz). However, the magnitude of $\lambda_{kr}(\omega_o,X_1)(=k_{re}(\omega_o,X_1)/k_{rn})$ is considered in two frequency regimes as illustrated in Fig. 7. The first curve-fit below Ω_1 (=2.5 Hz) is a linear function and the second one beyond Ω_1 (=2.5 Hz) is represented by a 5th order polynomial function. Two smoothening functions are

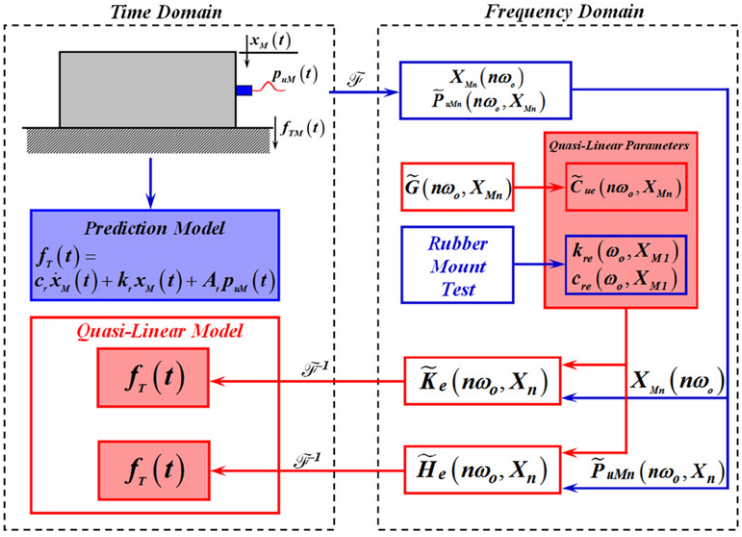

Fig. 6. Force estimation using quasi-linear models of Table 2. Key: $x_M(t)$, measured displacement; $p_{uM}(t)$, measured pressure; $\tilde{K}_e(n\omega_o,X_n)$, effective value of $\tilde{K}(n\omega_o,X_n)$; $\tilde{H}_e(n\omega_o,X_n)$, effective value of $\tilde{H}(n\omega_o,X_n)$; $f_T(t)$, force estimated by simple prediction model and quasi-linear models.

Table 1
'Virtual' excitation displacements X_n used for the quasi-linear (QL) model.

Experimental excitation, X (mm)		'Virtual' displacement (mm)				
		X_1	X_2	X_3	X_4	X_5
Fixed decoupler	0.15	0.15	4.1×10^{-4}	2.0×10^{-3}	4.4×10^{-4}	7.6×10^{-4}
	0.75	0.75	2.7×10^{-3}	8.7×10^{-3}	5.2×10^{-4}	1.8×10^{-3}
	1.5	1.5	6.8×10^{-3}	3.1×10^{-2}	3.4×10^{-3}	3.0×10^{-3}
Free decoupler	0.15	0.15	9.2×10^{-4}	9.6×10^{-4}	3.0×10^{-4}	1.8×10^{-4}
	0.75	0.75	4.3×10^{-3}	1.1×10^{-2}	4.3×10^{-4}	1.2×10^{-3}
	1.5	1.5	6.2×10^{-3}	3.2×10^{-2}	2.2×10^{-3}	4.0×10^{-3}

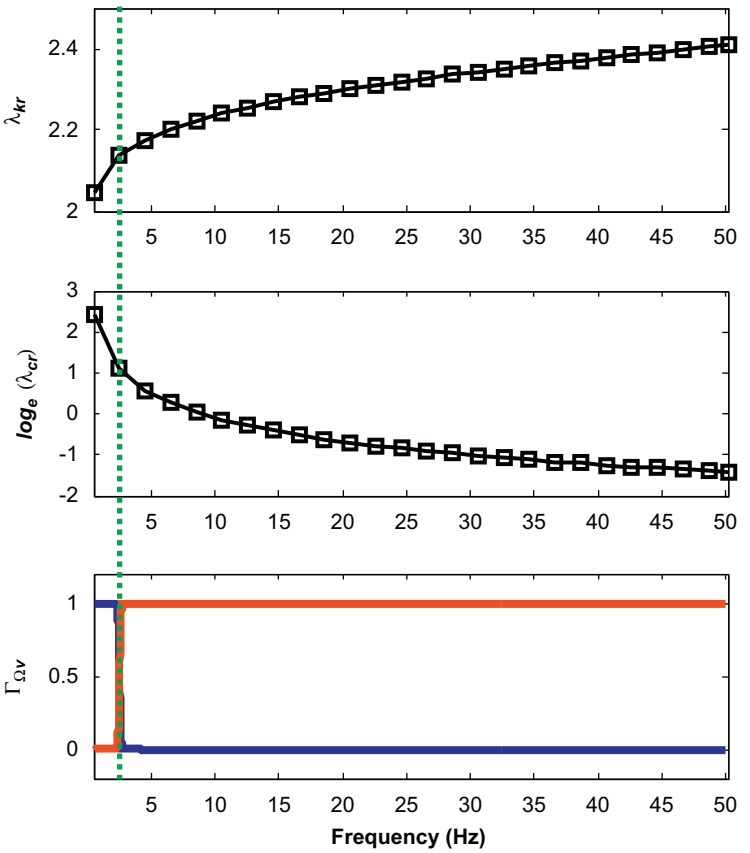

Fig. 7. Empirical parameters of the rubber path at X=0.15 mm. Here magnitudes of $\lambda_{kr}(\omega_o,X_1)$ and $\lambda_{cr}(\omega_o,X_1)$ are displayed along with the smoothening functions, $\Gamma_{\Omega v}$ (v=1, 2). The frequency regimes are separated at Ω_1=2.5 Hz. Key for $\Gamma_{\Omega v}$ curves: ——, $\Gamma_{\Omega 1}(\omega_o)$; ——, $\Gamma_{\Omega 2}(\omega_o)$.

employed in terms of $\Gamma_{\Omega 1}(\omega_o)$ and $\Gamma_{\Omega 2}(\omega_o)$ as shown in Fig. 7 [24] to yield the continuous profiles of $\lambda_{kr}(\omega_o,X_1)$:

$$k_{r1}(\omega_o) = a_{k1}(\omega_o/2\pi) + a_{k0}, \quad \Omega < \Omega_1, \tag{47}$$

$$k_{r2}(\omega_o) = b_{k5}(\omega_o/2\pi)^5 + b_{k4}(\omega_o/2\pi)^4 + b_{k3}(\omega_o/2\pi)^3 + b_{k2}(\omega_o/2\pi)^2 + b_{k1}(\omega_o/2\pi) + b_{k0}, \quad \Omega_1 < \Omega, \tag{48}$$

$$\Gamma_{\Omega 1}(\omega_o) = 0.5\{-\tanh[\sigma_1(\omega_o/2\pi - \Omega_1)] + 1\}, \tag{49}$$

$$\Gamma_{\Omega 2}(\omega_o) = 0.5\{\tanh[\sigma_2(\omega_o/2\pi - \Omega_2)] + 1\}. \tag{50}$$

Here, $k_{r1}(\omega_o)$ and $k_{r2}(\omega_o)$ are the curve-fits of $\lambda_{kr}(\omega_o,X_1)$ in the range of $\Omega < \Omega_1$ and $\Omega \geq \Omega_1$, respectively, and, $\Gamma_{\Omega 1}(\omega_o)$ and $\Gamma_{\Omega 2}(\omega_o)$ are the smoothening functions over $\Omega < \Omega_1$ and $\Omega \geq \Omega_1$ regimes, respectively. The smoothening factors σ_v (v=1–2) are selected as $\sigma_1=\sigma_2=1\times10^6$. In our study, the coefficients a_{kv}(v=0, 1) and b_{kv} (v=0–5) are determined corresponding to each excitation X. For example, a_{k1}=0.045, 0.038, 0.036, 0.034, 0.0324, 0.033, and 0.030 with X=0.15, 0.25, 0.5, 0.75, 1.0, 1.25, and 1.5 mm respectively; a_{k0}=2.03, 2.02, 1.96, 1.92, 1.89, 1.86, and 1.85 with X=0.15, 0.25, 0.5, 0.75, 1.0, 1.25, and

1.5 mm, respectively. Likewise, 6 sets of coefficients for b_{kv} (v=0–5) are estimated corresponding to X=0.15, 0.25, 0.5, 0.75, 1.0, 1.25, and 1.5 mm. Thus, another set of curve-fits with respect to X_1 is used as follows:

$$a_{kv}(X_1) = \sum_{w=1}^{7} a_{kvw-1} {X_1}^{w-1} (v = 0,1), \tag{51}$$

$$b_{kv}(X_1) = \sum_{w=1}^{7} b_{kvw-1} {X_1}^{w-1} (v = 0{-}5), \tag{52}$$

$$a_{k1}(X_1) = a_{k16}X_1^6 + a_{k15}X_1^5 + a_{k14}X_1^4 + a_{k13}X_1^3 + a_{k12}X_1^2 + a_{k11}X_1 + a_{k10}. \tag{53}$$

Here, $a_{kv}(X_1)$ and $b_{kv}(X_1)$ are the coefficient curve-fits for a_{kv}(v=1, 0) and b_{kv} (v=0–5) with the function of X_1, respectively. Eq. (53) describes a typical example of coefficient curve-fit as a function of X. Sample coefficients a_{k1w-1} are as follows: a_{16}=0.098; a_{15}=−0.596; a_{14}=1.411; a_{13}=−1.652; a_{12}=1.003; a_{11}=−0.304; a_{10}=0.073. Therefore, the overall procedure to determine the spectrally varying and amplitude-sensitive parameters for $\lambda_{kr}(\omega_o,X_1)$ is described as follows:

$$k_{re}(\omega_o,X_1) = k_{rn}\lambda_{kr}(\omega_o,X_1), \tag{54}$$

$$\lambda_{kr}(\omega_o,X_1) = k_{\Omega 1}(\omega_o,X_1) + k_{\Omega 2}(\omega_o,X_1), \tag{55}$$

$$k_{\Omega 1}(\omega_o,X_1) = k_{r1}(\omega_o,X_1)\Gamma_{\Omega 1}(\omega_o), \tag{56}$$

$$k_{\Omega 2}(\omega_o,X_1) = k_{r2}(\omega_o,X_1)\Gamma_{\Omega 2}(\omega_o), \tag{57}$$

$$k_{r1}(\omega_o,X_1) = a_{k1}(X_1)(\omega_o/2\pi) + a_{k0}(X_1), \tag{58}$$

$$k_{r2}(\omega_o,X_1) = b_{k5}(X_1)(\omega_o/2\pi)^5 + b_{k4}(X_1)(\omega_o/2\pi)^4 + b_{k3}(X_1)(\omega_o/2\pi)^3 + b_{k2}(X_1)(\omega_o/2\pi)^2 + b_{k1}(X_1)(\omega_o/2\pi) + b_{k0}(X_1). \tag{59}$$

Here, $k_{\Omega v}(\omega_o,X_1)$ (v=1, 2) is the smoothened function of $k_{rv}(\omega_o,X_1)$ (v=1, 2) and $k_{rv}(\omega_o,X_1)$ (v=1, 2) is the polynomial curve-fit in the relevant frequency range. The coefficients a_{kv} (v=0, 1) and b_{kv} (v=0–5) are described in Eqs. (51) to (53). Similarly, $\lambda_{cr}(\omega_o,X_1)$=$c_{re}(\omega_o,X_1)/c_{rn}$ is estimated as follows. Note that $\lambda_{cr}(\omega_o,X_1)$ is now considered on a $\log_e$ scale, as indicated below, since the damping varies over a large range:

$$c_{re}(\omega_o,X_1) = c_{rn}e^{\lambda_{kr}(\omega_o,X_1)}, \tag{60}$$

$$\lambda_{cr}(\omega_o,X_1) = c_{\Omega 1}(\omega_o,X_1) + c_{\Omega 2}(\omega_o,X_1), \tag{61}$$

$$c_{\Omega 1}(\omega_o,X_1) = c_{r1}(\omega_o,X_1)\Gamma_{\Omega 1}(\omega_o), \tag{62}$$

$$c_{\Omega 2}(\omega_o,X_1) = c_{r2}(\omega_o,X_1)\Gamma_{\Omega 2}(\omega_o), \tag{63}$$

$$c_{r1}(\omega_o,X_1) = a_{c1}(X_1)(\omega_o/2\pi) + a_{c0}(X_1), \tag{64}$$

$$c_{r2}(\omega_o,X_1) = b_{c5}(X_1)(\omega_o/2\pi)^5 + b_{c4}(X_1)(\omega_o/2\pi)^4 + b_{c3}(X_1)(\omega_o/2\pi)^3 + b_{c2}(X_1)(\omega_o/2\pi)^2 + b_{c1}(X_1)(\omega_o/2\pi) + b_{c0}(X_1). \tag{65}$$

Likewise, $c_{\Omega v}(\omega_o,X_1)$ (v=1, 2) is the smoothened function of $c_{rv}(\omega_o,X_1)$ (v=1, 2) and $c_{rv}(\omega_o,X_1)$ (v=1, 2) is the polynomial curve-fit in the relevant frequency range. Again, a_{cv} (v=0, 1) and b_{cv} (v=0–5) are also calculated using the method described by Eqs. (51)–(53). Finally, the estimated $\lambda_{kr}(\omega_o,X_1)$ and $\lambda_{cr}(\omega_o,X_1)$ are embedded in the quasi-linear model at the fundamental harmonic term (ω_o).

6.3. Effective hydraulic force path parameter $\tilde{\lambda}_u(n\omega_o,X_n)$ at super-harmonics

The effective dynamic compliance $\tilde{C}_{ue}(n\omega_o,X_n)$ is next evaluated at the super-harmonics ($n\omega_o$). Note that the term X_n should be viewed as the 'virtual' excitation displacement amplitude at $n\omega_o$. Even though $x(t)$ is close to a pure sinusoid, super-harmonic amplitudes X_n are observed via the FFT analysis of $x_M(t)$ signals even though their amplitudes are several orders of magnitudes lower, as listed in Table 1. These can be employed to estimate $\tilde{C}_{ue}(n\omega_o,X_n)$ in terms of $\tilde{\lambda}_u(n\omega_o,X_n)(=\alpha_n+i\beta_n)$ as follows where C_{un} is the nominal (static) value:

$$\tilde{C}_{ue}(n\omega_o,X_n) = C_{un}\tilde{\lambda}_u(n\omega_o,X_n) = C_{un}(\alpha_n + i\beta_n), \tag{66}$$

$$\beta_n = \beta(n\omega_o,X_n), (n = 1,2,3,\ldots), \quad \alpha_n = \alpha(n\omega_o,X_n). \tag{67}$$

From Eqs. (9) to (13), the relationship between $X(s)$ and $P_u(s)$ is derived as follows for the fixed decoupler mount (with $I_d \approx 0$ and $R_d \to \infty$) under the steady state condition. The complex valued terms $\tilde{P}_u(n\omega_o,X_n)$ at n=1,2,3,… are expressed in

the frequency domain (with multi-harmonic terms) by replacing s with $i(n\omega_o)$:

$$\tilde{P}_u(n\omega_o,X_n)=\frac{A_r\left[\left(1-(n\omega_o)^2C_lI_i\right)+i(n\omega_o)C_lR_i\right]X_n}{\left(C_u+C_l-(n\omega_o)^2C_uC_lI_i\right)+i(n\omega_o)C_uC_lR_i}\quad(n=1,2,3,\ldots). \tag{68}$$

From Eqs. (66) and (67), $\tilde{\lambda}_u(n\omega_o,X_n)$ can be related in terms of α_n and β_n in the frequency domain at the $n\omega_o$ terms, and this step leads to:

$$\begin{aligned}\tilde{P}_u(n\omega_o,X_n)&=\frac{A_r\left[(1-(n\omega_o)^2C_lI_i)+i(n\omega_o)C_lR_i\right]X_n}{\left[\lambda_uC_{un}+C_l-(n\omega_o)^2C_lI_i(\lambda_uC_{un})\right]+i(n\omega_o)C_lR_i(\lambda_uC_{un})}\\&=\frac{A_r\left[(1-(n\omega_o)^2C_lI_i)+i(n\omega_o)C_lR_i\right]X_n}{\left[(\alpha_n+i\beta_n)C_{un}+C_l-(n\omega_o)^2C_lI_i(\alpha_n+i\beta_n)C_{un}\right]+i(n\omega_o)C_lR_i(\alpha_n+i\beta_n)C_{un}}\end{aligned} \tag{69}$$

The measured $\tilde{P}_{uM}(n\omega_o,X_n)$ signal is considered as a complex quantity and given by magitude $\left|\tilde{P}_{uMn}\right|$ and phase ϕ_{Mn} as

$$\tilde{P}_{uMn}=P_{uREn}+iP_{uIMn}, \tag{70}$$

$$P_{uREn}=Re\left[\tilde{P}_{uMn}\right]=\left|\tilde{P}_{uMn}\right|\cos(\phi_{Mn}), \tag{71}$$

$$P_{uIMn}=Im\left[\tilde{P}_{uMn}\right]=\left|\tilde{P}_{uMn}\right|\sin(\phi_{Mn}). \tag{72}$$

From Eqs. (69) and (70), the empirical coeffifinets α_n and β_n are determined at $n\omega_o$ and X_n as follows:

$$P_{uREn}+iP_{uIMn}=\frac{A_r\left[\left(1-(n\omega_o)^2C_lI_i\right)+i(n\omega_o)C_lR_i\right]X_n}{\left[\left(C_{un}-(n\omega_o)^2C_lC_{un}I_i\right)\alpha_n-(C_lC_{un}R_i(n\omega_o))\beta_n+C_l\right]+i\left[(C_lC_{un}R_i(n\omega_o))\alpha_n+\left(C_{un}-(n\omega_o)^2C_lC_{un}I_i\right)\beta_n\right]}, \tag{73}$$

$$\alpha_n=\frac{\alpha_{n4}(n\omega_o)^4+\alpha_{n2}(n\omega_o)^2+\alpha_{n0}}{d_{n4}(n\omega_o)^4+d_{n2}(n\omega_o)^2+d_{n0}}, \tag{74}$$

$$\beta_n=\frac{\beta_{n4}(n\omega_o)^4+\beta_{n2}(n\omega_o)^2+\beta_{n1}(n\omega_o)+\beta_{n0}}{d_{n4}(n\omega_o)^4+d_{n2}(n\omega_o)^2+d_{n0}}, \tag{75}$$

$$\alpha_{n4}=X_nA_rC_l^2I_i^2P_{uREn}, \tag{76}$$

$$\alpha_{n2}=X_nA_rP_{uREn}C_l\left(C_lR_i^2-2I_i\right)+C_l^2\left(P_{uREn}^2+P_{uIMn}^2\right)I_i, \tag{77}$$

$$\alpha_{n0}=X_nA_rP_{uREn}-C_l\left(P_{uREn}^2+P_{uIMn}^2\right), \tag{78}$$

$$\beta_{n4}=-X_nA_rC_l^2I_i^2P_{uIMn}, \tag{79}$$

$$\beta_{n2}=X_nA_rP_{uIMn}C_l\left(2I_i-C_lR_i^2\right), \tag{80}$$

$$\beta_{n1}=C_l^2\left(P_{uREn}^2+P_{uIMn}^2\right)R_i, \tag{81}$$

$$\beta_{n0}=-X_nA_rP_{uIMn}, \tag{82}$$

$$d_{n4}=C_{un}C_l^2I_i^2\left(P_{uREn}^2+P_{uIMn}^2\right), \tag{83}$$

$$d_{n2}=C_{un}C_l\left(C_lR_i^2-2I_i\right)\left(P_{uREn}^2+P_{uIMn}^2\right), \tag{84}$$

$$d_{n0}=C_{un}\left(P_{uREn}^2+P_{uIMn}^2\right). \tag{85}$$

Here, the subscripts RE and IM designate the real and imaginary numbers, respectively. Simillary, expressions for the free decoupler mount (with assumptions such as $I_d\approx 0$ below 50 Hz) are derived leading to

$$\widetilde{P}_u(n\omega_o,X_n)=\frac{X_nA_r\left[-(n\omega_o)^2C_lI_iR_d+i(n\omega_o)(C_lR_iR_d+I_i)+(R_i+R_d)\right]}{-(n\omega_o)^2C_uC_lI_iR_d+i(n\omega_o)[C_uC_lR_iR_d+(C_u+C_l)I_i]+(C_u+C_l)(R_i+R_d)}, \tag{86}$$

$$\alpha_n=\frac{\alpha_{n4}(n\omega_o)^4+\alpha_{n2}(n\omega_o)^2+\alpha_{n0}}{d_{n4}(n\omega_o)^4+d_{n2}(n\omega_o)^2+d_{n0}}, \tag{87}$$

$$\beta_n = \frac{\beta_{n4}(n\omega_o)^4 + \beta_{n3}(n\omega_o)^3 + \beta_{n2}(n\omega_o)^2 + \beta_{n1}(n\omega_o) + \beta_{n0}}{d_{n4}(n\omega_o)^4 + d_{n2}(n\omega_o)^2 + d_{n0}}, \tag{88}$$

$$\alpha_{n4} = X_n A_r P_{uREn} C_{un} C_l^2 I_i^2 R_d^2, \tag{89}$$

$$\alpha_{n2} = X_n A_r P_{uREn} C_{un} C_l^2 R_i^2 R_d^2 + \left[C_l\left(P_{uREn}^2 + P_{ulMn}^2\right) - 2X_n A_r P_{uREn}\right] C_{un} C_l I_i R_d^2 + \left[X_n A_r P_{uREn} - C_l\left(P_{uREn}^2 + P_{ulMn}^2\right)\right] C_{un} I_i^2, \tag{90}$$

$$\alpha_{n0} = C_{un}\left[X_n A_r P_{uREn} - C_l\left(P_{uREn}^2 + P_{ulMn}^2\right)\right](R_i + R_d)^2, \tag{91}$$

$$\beta_{n4} = -X_n A_r P_{ulMn} C_{un} C_l^2 I_i^2 R_d^2, \tag{92}$$

$$\beta_{n3} = C_{un} C_l^2 \left(P_{uREn}^2 + P_{ulMn}^2\right) I_i^2 R_d, \tag{93}$$

$$\beta_{n2} = -X_n A_r P_{ulMn} C_{un}\left[C_l^2 R_i^2 R_d^2 - 2C_l I_i R_d^2 + I_i^2\right], \tag{94}$$

$$\beta_{n1} = C_{un} C_l^2 R_i R_d \left(P_{uREn}^2 + P_{ulMn}^2\right)(R_i + R_d), \tag{95}$$

$$\beta_{n0} = -X_n A_r P_{ulMn} C_{un}(R_i + R_d)^2, \tag{96}$$

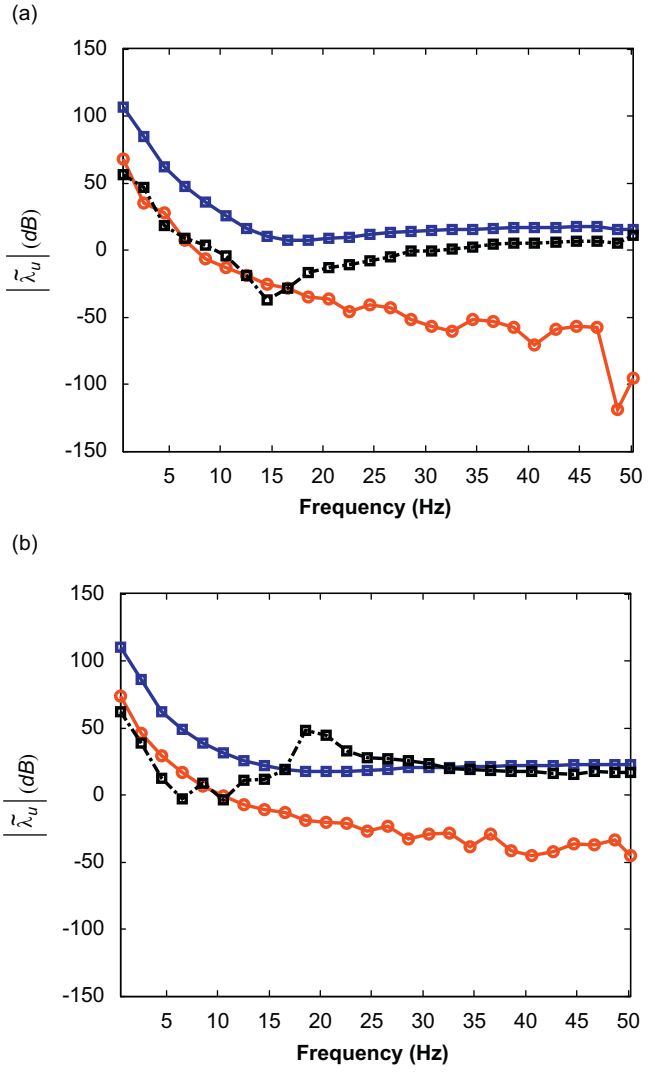

Fig. 8. Effective parameter for the upper chamber compliance, displayed in terms of the magnitude spectra of $20\mathrm{Log}_e|\tilde{\lambda}_u(n\omega_o, X_n)|$ *re* $\lambda_u = 1.0$ dB with three harmonic terms given X=1.5 mm: (a) fixed decoupler mount and (b) free decoupler mount. Key: —□—, n=1; —○—, n=2; —·□·—, n=3.

$$d_{n4} = (P_{uREn}^2 + P_{ulMn}^2) C_{un}^2 C_l^2 I_i^2 R_d^2, \tag{97}$$

$$d_{n2} = C_{un}^2 (P_{uREn}^2 + P_{ulMn}^2) [C_l^2 R_i^2 R_d^2 - 2C_l I_i R_d^2 + I_i^2], \tag{98}$$

$$d_{n0} = C_{un}^2 (P_{uREn}^2 + P_{ulMn}^2)(R_i + R_d)^2. \tag{99}$$

Fig. 8 compares the magnitude spectra of $\tilde{\lambda}_u(n\omega_o, X_n)$ based upon Eqs. (66), (67), (74)–(85), and (87)–(99) up to $n=3$ term with given excitation $X=1.5$ mm. When the results of both fixed and free decouplers are compared with those with the fundamental ω_o only, dynamic characteristics seem to show similar responses. But, the magnitudes of 2nd and 3rd harmonics show mount specific behavior. This illustrates the importance of nonlinear dynamics. For instance, the $\tilde{\lambda}_u(n\omega_o, X_n)$ spectra for the free decoupler mount show higher magnitudes around 20 Hz for the 3rd harmonic term, when compared with results at ω_o. This is directly related to the switching mechanism as well as the nonlinear upper chamber compliance [19,20].

7. Examination of super-harmonics and estimation of forces in time domain

7.1. Examination of super-harmonics in measured data

Typical $p_{uM}(t)$ and $f_{TM}(t)$ measurements for the free decoupler mount at 8.5 Hz (with $X=1.5$ mm) are shown in Figs. 9(a), (b) and Fig. 10(a). Spectral contents are determined by the FFT algorithm as shown in Fig. 10(b). Even though the fundamental ω_o term (8.5 Hz) is quite dominant, responses reveal several $n\omega_o$ terms (especially the second harmonic at 17 Hz and third harmonic at 25.5 Hz). Also, spectral contents of $f_{TM}(t)$ are similar to those of $p_{uM}(t)$. Therefore, the super-harmonic terms in $f_{TM}(t)$ can be assumed to be controlled by the nonlinear characteristics of the hydraulic path.

Figs. 11 and 12 map the magnitude spectra of $\tilde{P}_{uM}(n\omega_o, X)$ and $\tilde{F}_{TM}(n\omega_o, X)$, respectively, up to 3rd harmonic term for the fixed decoupler mount up to 50 Hz with $X=1.5$ mm. When the contents at ω_o are compared with those at $n\omega_o$ in Fig. 11(a) and (b), the magnitude of the ω_o term is dominant as observed in Fig. 10(b) as well. Also, the super-harmonic contents of $\tilde{F}_{TM}(n\omega_o, X)$ seem to match the $\tilde{P}_{uM}(n\omega_o, X)$ spectra in Fig. 11(a), (b) and 12. This is further investigated in the time domain by marking key events in Fig. 10(a) as "A" and "B". Note that the fundamental $\tilde{F}_{TM}(n\omega_o, X)$ term is also dependent upon the initial conditions.

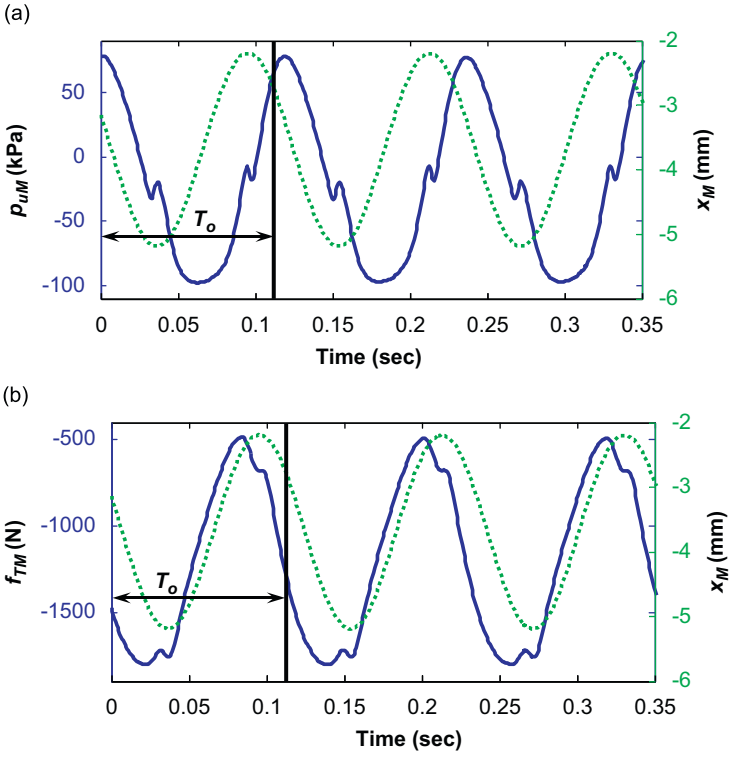

Fig. 9. $p_{uM}(t)$ and $f_{TM}(t)$ for the free decoupler mount given $X=1.5$ mm, $\varphi_X=68.7^\circ$ and $\omega_o/2\pi=8.5$ Hz: (a) time history of $p_{uM}(t)$; (b) time history of $f_{TM}(t)$. Key: ·····, $x_M(t)$; ——, $p_{uM}(t)$ and $f_{TM}(t)$; T_o, period ($=2\pi/\omega_o$).

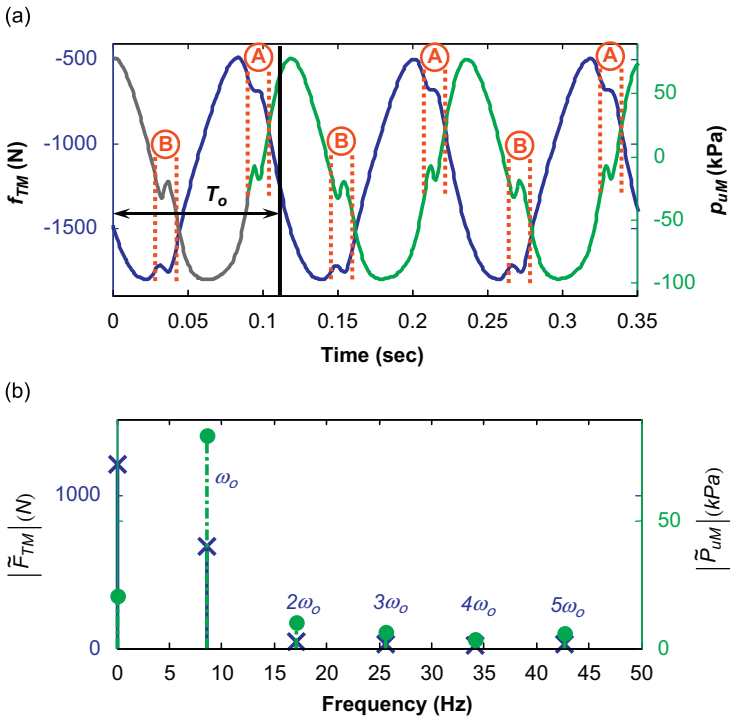

Fig. 10. Measured pressure (and force) time histories and spectra for the free decoupler mount given X=1.5 mm, φ_X=68.7° and $\omega_o/2\pi$=8.5 Hz: (a) time history of $p_{uM}(t)$ and $f_{TM}(t)$; (b) magnitude spectra ($\tilde{P}_{uM}$ and $\tilde{F}_{TM}$). Key for part (a) ——, $p_{uM}(t)$; ——, $f_{TM}(t)$; T_o, period (=$2\pi/\omega_o$). Key for part (b) -×-, $|\tilde{F}_{TM}|$; -●-, $|\tilde{P}_{uM}|$.

7.2. *Indirect force estimation given measured $X_{Mn}(n\omega_o)$ and $\tilde{P}_{uMn}(n\omega_o,X_n)$*

Based on the experimental data, we assume that the $n\omega_o$ contents of $f_T(t)$ and $\tilde{F}_T(n\omega_o,X)$ are directly affected by the corresponding terms of $p_u(t)$ and $\tilde{P}_{uM}(n\omega_o,X)$. Thus, all $n\omega_o$ terms are lumped into the hydraulic path. This premise is employed for estimating $\tilde{C}_{ue}(n\omega_o,X)$. Further, the Fourier series expansion is utilized by employing the reverse path spectral method that has been well described by Richards and Singh [25], and Bendat [26].

Fig. 6 illustrates the procedure used to estimate the dynamic forces given measured $x_M(t)$ and $p_{uM}(t)$ signals under harmonic excitation at ω_o. The $x_M(t)$ and $p_{uM}(t)$ time histories are then transformed into $X_{Mn}(n\omega_o)$ and $\tilde{P}_{uMn}(n\omega_o,X_{Mn})$, respectively, where $X_{Mn}(n\omega_o)$ is viewed as the 'virtual' sinusoidal input and $\tilde{P}_{uMn}(n\omega_o,X_{Mn})$ includes relevant $n\omega_o$ terms. Second, effective parameters from both rubber and hydraulic paths are identified, as illustrated in Fig. 13, by employing the reverse path spectral method [25,26]. For example, $\tilde{C}_{ue}(n\omega_o,X_{Mn})$ is calculated by Eqs. (66)–(99) for both fixed and free decoupler mounts. When the measured amplitudes $\tilde{P}_{uMn}(n\omega_o,X_{Mn})$ are employed in Eqs. (66)–(99), $\tilde{C}_{ue}(n\omega_o,X_{Mn})$ should be given at $n\omega_o$ such as $\tilde{C}_{ue}(n\omega_o,X_{M1})$ from $\tilde{P}_{uM1}(n\omega_o,X_{M1})$ and $\tilde{C}_{ue}(n\omega_o,X_{M2})$ from $\tilde{P}_{uM2}(n\omega_o,X_{M2})$. Next, the quasi-linear transfer functions $\tilde{G}_e(n\omega_o,X_{Mn})=(k_{rref}/A_r)\overline{G}(n\omega_o,X_{Mn})$ are used, as described in Fig. 13(a), at $n\omega_o$ terms corresponding to $X_{Mn}(n\omega_o)$ and $\tilde{P}_{uMn}(n\omega_o,X_{Mn})$. Also, as illustrated in Fig. 13(b), $k_{re}(\omega_o,X_1)$ and $c_{re}(\omega_o,X_1)$ are identified by using $X_{M1}(\omega_o)$ at ω_o as described by Eqs. (54)–(65). Further, other transfer functions such as $\tilde{K}(n\omega_o,X_n)=k_{rref}\overline{K}(n\omega_o,X_n)$ and $\tilde{H}(n\omega_o,X_n)=A_r\overline{H}(n\omega_o,X_n)$ from Eqs. (14) to (33) are now used to estimate the dynamic forces at $n\omega_o$ terms. The overall procedure with effective parameters $k_{re}(\omega_o,X_1)$, $c_{re}(\omega_o,X_1)$ and $\tilde{C}_{ue}(n\omega_o,X_n)$ is illustrated in Figs. 6 and 14. In particular, Fig. 14 describes the reverse path spectral method which employs effective parameters of Fig. 13. Thus, $\tilde{K}_e(n\omega_o,X_n)$ and $\tilde{H}_e(n\omega_o,X_n)$ assume effective values at each $n\omega_o$ term since both are affected by $\tilde{C}_{ue}(n\omega_o,X_n)$.

8. Force estimations with quasi-linear models

Alternate force estimation schemes are summarized in Table 2, especially for the quasi-linear (QL) model that depends upon the empirical parameters $\lambda_{kr}(\omega_o,X_1)$, $\lambda_{cr}(\omega_o,X_1)$, and $\tilde{\lambda}_u(n\omega_o,X_n)$. When $\lambda_{kr}(\omega_o,X_1)=1$, $\lambda_{cr}(\omega_o,X_1)=1$, and $\tilde{\lambda}_u(n\omega_o,X_n)=1$, then the model is obviously linear time-invariant (LTI) with nominal values of k_r, c_r, and C_u as described earlier in Sections 2 and 3. The LTI model (with calculated $x(t)$ and $p_u(t)$) is designated as I-A in Table 2; note that it is equivalent to the 'simple prediction model' that employs measured $x_M(t)$ and $p_{uM}(t)$. As illustrated in Table 2, many different calculation schemes can be designed based on the combination of $\lambda_{kr}(\omega_o,X_1)$, $\lambda_{cr}(\omega_o,X_1)$ and $\tilde{\lambda}_u(n\omega_o,X_n)$ along with applicable transfer

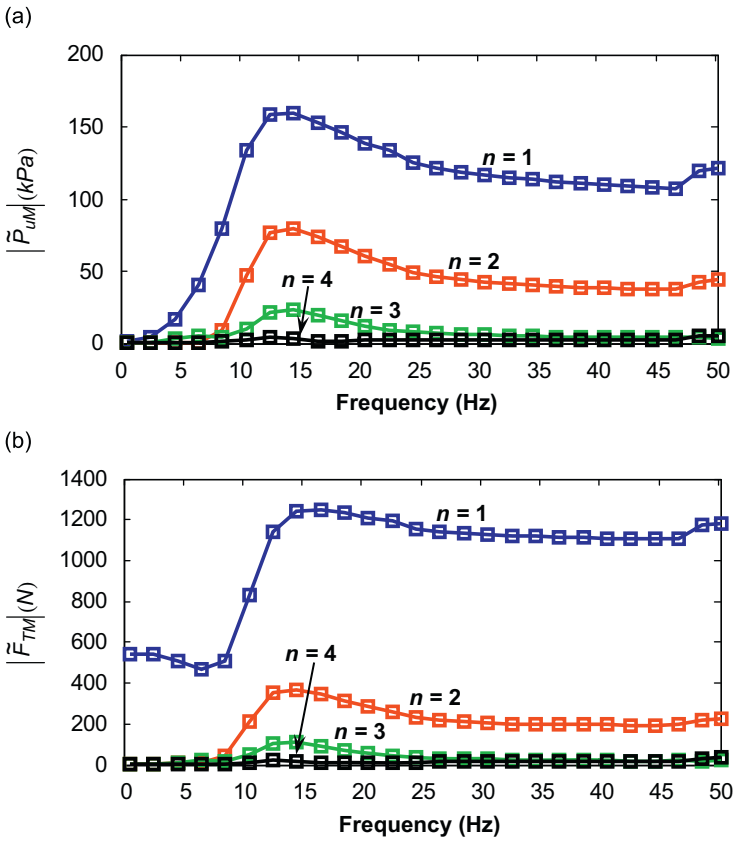

Fig. 11. Magnitude spectra of $\tilde{P}_{uM}$ and $\tilde{F}_{TM}$ for the fixed decoupler mount given X=1.5 mm: (a) magnitude of $\tilde{P}_{uM}$ with four harmonic terms; (b) magnitude of $\tilde{F}_{TM}$ with four harmonic terms. Key: —⊟—, 1st harmonic; —⊟—, 2nd harmonic; —⊟—, 3rd harmonic; and —⊡—, 4th harmonic.

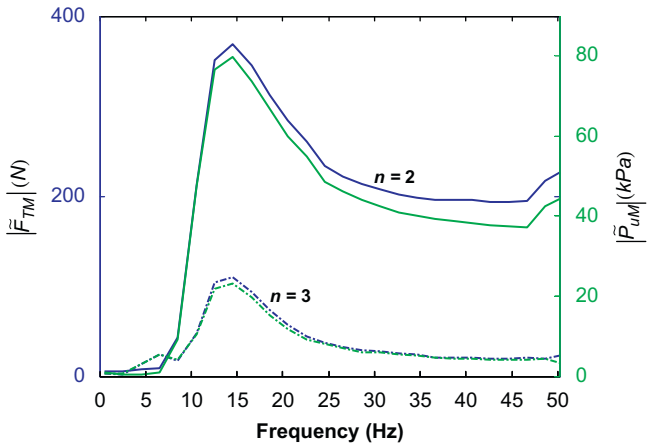

Fig. 12. Magnitude spectra of $\tilde{P}_{uM}$ and $\tilde{F}_{TM}$ for the fixed decoupler mount given X=1.5 mm. Key: ——, 2nd harmonic of $|\tilde{F}_{TM}(\omega,X)|$; ——, 2nd harmonic of $|\tilde{P}_{uM}(\omega,X)|$; - - -, 3rd harmonic of $|\tilde{F}_{TM}(\omega,X)|$; - - -, 3rd harmonic of $|\tilde{P}_{uM}(\omega,X)|$.

functions such as $\tilde{K}_e(n\omega_o,X_n)$ for schemes II-A, II-B, and II-C, $\tilde{H}_e(n\omega_o,X_n)$ for schemes III-A, III-B, and III-C, or $\tilde{K}_{Ae}(n\omega_o,X_n)$ for schemes IV-A and IV-B. Finally, observe that the nonlinear model (NL) employs nominal nonlinear parameters as described in Section 5, and thus effective (frequency domain) parameters are not considered in this formulation.

In order to estimate $f_T(t)$ from a transfer function $\tilde{K}_e$ or $\tilde{H}_e$ with effective k_{re}, c_{re} and $\tilde{C}_{ue}$, the Fourier series expansion is employed for particular QL schemes as illustrated below. Assuming that the mount is excited under steady state condition, define the input displacement $x(t)$ as $\mathrm{Re}[\tilde{X}_n e^{i\omega_n t}] = \mathrm{Re}[X_n e^{i(\omega_n t+\varphi_{Xn})}]$. Note that the 'virtual' sinusoidal inputs at $n\omega_o$ are included where X_n and φ_{Xn} are the amplitude and phase at the nth harmonic. First, the dynamic force is estimated at n=1 or

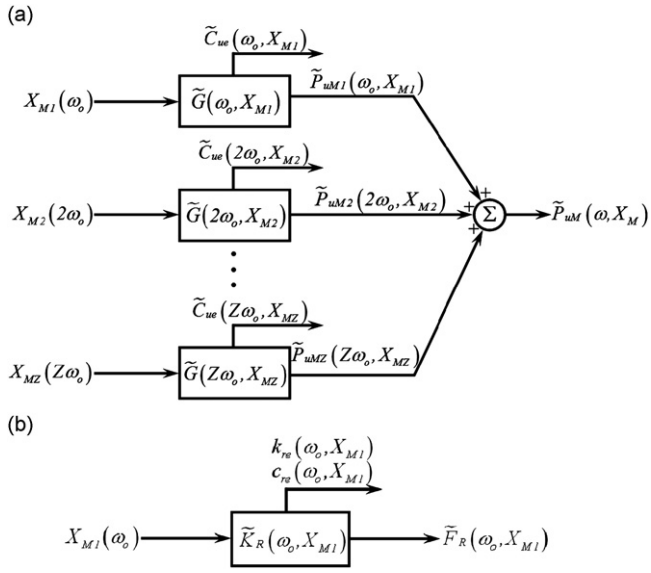

Fig. 13. Identification of effective parameters for the reverse path spectral method: (a) identification of effective upper chamber compliance ($\tilde{C}_{ue}$) with multi-harmonic terms and (b) identification of effective stiffness (k_{re}) and damping (c_{re}) with fundamental harmonic term. Key: $\tilde{K}_R(\omega_o, X_{M1})$, dynamic stiffness from the rubber path; $\tilde{F}_R(\omega_o, X_{M1})$, rubber path force.

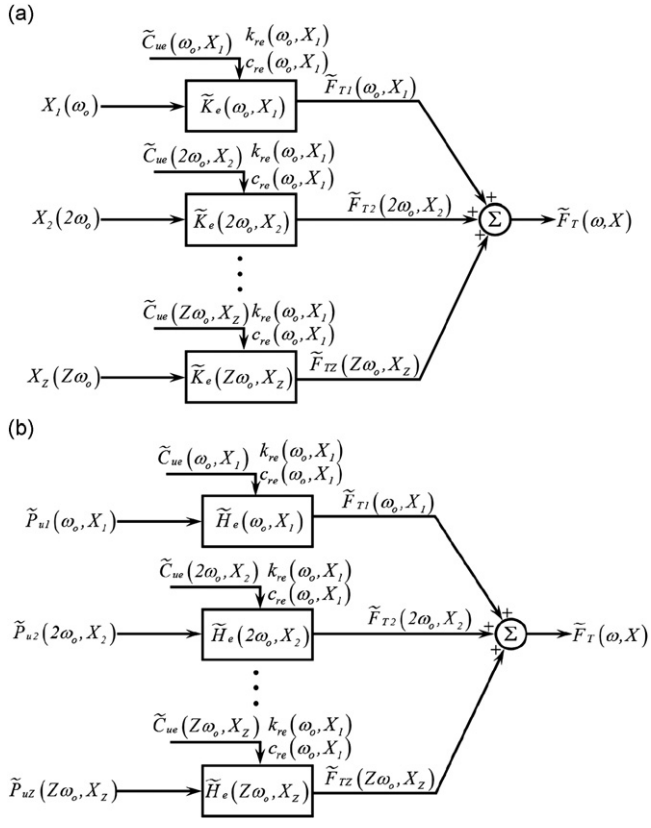

Fig. 14. Force estimation in frequency domain using the reverse path spectral method: (a) dynamic stiffness ($\tilde{K}_e$) concept and (b) force transmissibility ($\tilde{H}_e$) concept.

Table 2
Overview of linear, quasi-linear and nonlinear models used to estimate dynamic forces.

Model and scheme designation		Sensor(s) or variables required		Spectrally varying and amplitude-sensitive parameters	Harmonic content
		$x(t)$	$p_u(t)$		
Fluid system model (Fig. 1)					
Simple prediction model given measured data		Yes	Yes	$\tilde{\lambda}_{kr}=1,\ \tilde{\lambda}_{cr}=1$	ω_o only
***Nonlinear model* (*NL*)**		Yes	No	$\tilde{\lambda}_{kr}=1,\ \tilde{\lambda}_{cr}=1$	$n\omega_o$ (n=1,2,3, …)
***Linear time-invariant model* (*LTI*)**					
I-A		Yes	Yes	$\tilde{\lambda}_{kr}=1,\ \tilde{\lambda}_{cr}=1$	ω_o only
***Quasi-linear model* (*QL*)**	***I-B***	Yes	Yes	$\tilde{\lambda}_{kr}\neq 1,\ \tilde{\lambda}_{cr}\neq 1$	$n\omega_o$ (n=1,2,3, …)
	II-A	Yes	No	$\tilde{\lambda}_{kr}=1,\ \tilde{\lambda}_{cr}=1,\ \tilde{\lambda}_{u}\neq 1$	
	II-B	Yes	No	$\tilde{\lambda}_{kr}\neq 1,\ \tilde{\lambda}_{cr}\neq 1,\ \tilde{\lambda}_{u}=1$	
	II-C	Yes	No	$\tilde{\lambda}_{kr}\neq 1,\ \tilde{\lambda}_{cr}\neq 1,\ \tilde{\lambda}_{u}\neq 1$	
	III-A	No	Yes	$\tilde{\lambda}_{kr}=1,\ \tilde{\lambda}_{cr}=1,\ \tilde{\lambda}_{u}\neq 1$	
	III-B	No	Yes	$\tilde{\lambda}_{kr}\neq 1,\ \tilde{\lambda}_{cr}\neq 1,\ \tilde{\lambda}_{u}=1$	
	III-C	No	Yes	$\tilde{\lambda}_{kr}=1,\ \tilde{\lambda}_{cr}\neq 1,\ \tilde{\lambda}_{u}\neq 1$	
Analogous mechanical system model (Fig. 3)					
***Linear time-invariant model* (*LTI*)**	***IV-A***	Yes	No	$\tilde{\lambda}_{kr}=1,\ \tilde{\lambda}_{cr}=1,\ \tilde{\lambda}_{u}=1$	ω_o only
***Quasi-linear model* (*QL*)**	***IV-B***	Yes	No	$\tilde{\lambda}_{kr}\neq 1,\ \tilde{\lambda}_{cr}\neq 1,\ \tilde{\lambda}_{u}\neq 1$	$n\omega_o$ (n=1,2,3, …)

ω_o term as described below where the subscripts L, K, and H indicate the LTI model, dynamic stiffness $\tilde{K}_e(\omega_o,X_1)$, and force transmissibility $\tilde{H}_e(\omega_o,X_1)$ formulations. respectively:

$$\chi_{KL}=k_{\mathrm{ref}}X_{\mathrm{ref}},\quad \chi_{HL}=A_rP_u(\omega_o,X_1), \tag{100}$$

$$p_u(t)=\mathrm{Re}[\tilde{P}_{un}e^{i\omega_o t}]=\mathrm{Re}[P_{un}e^{i(\omega_o t+\varphi_{Pun})}], \tag{101}$$

$$f_{TKL}(t)=f_m+\chi_{KL}\left|\overline{K}_e(\omega_o,X_1)\right|\mathrm{Re}\left[e^{i(\omega_o t+\varphi_{X1}+\varphi_{KL})}\right],\quad \varphi_{KL}(\omega_o)=\angle\overline{K}_e(\omega_o,X_1), \tag{102}$$

$$f_{THL}(t)=f_m+\chi_{HL}\left|\overline{H}_e(\omega_o,X_1)\right|\mathrm{Re}\left[e^{i(\omega_o t+\varphi_{Pu1}+\varphi_{HL})}\right],\quad \varphi_{HL}(\omega_o)=\angle\overline{H}_e(\omega_o,X_1). \tag{103}$$

Here, φ_{Pun} is the phase of $p_u(t)$ at $n\omega_o$ term, φ_{KL} is the phase of $\tilde{K}_e(\omega_o,X_1)$, and φ_{HL} is the phase of $\tilde{H}_e(\omega_o,X_1)$. The above models include measured X_{M1} and $\tilde{P}_{uM1}$ contents at ω_o with X_1. Next, the time domain force is constructed by using QL models at relevant n terms as follows:

$$f_{TKQ}(t)=f_m+f_{TKQ1}(t)+f_{TKQ2}(t)+\cdots+f_{TKQZ}(t), \tag{104}$$

$$f_{TKQ1}(t)=\chi_{KL}\left|\overline{K}_e(\omega_o,X_1)\right|\mathrm{Re}\left[e^{i[\omega_o t+\varphi_{X1}+\varphi_{KQ}(\omega_o,X_1)]}\right], \tag{105}$$

$$f_{TKQ2}(t)=\chi_{KL}\left|\overline{K}_e(2\omega_o,X_2)\right|\mathrm{Re}\left[e^{i[2\omega_o t+\varphi_{X2}+\varphi_{KQ}(2\omega_o,X_2)]}\right], \tag{106}$$

$$f_{TKQZ}(t)=\chi_{KL}\left|\overline{K}_e(Z\omega_o,X_Z)\right|\mathrm{Re}\left[e^{i[Z\omega_o t+\varphi_{XZ}+\varphi_{KQ}(Z\omega_o,X_Z)]}\right], \tag{107}$$

$$\varphi_{KQ}(n\omega_o,X_n)=\angle\overline{K}_e(n\omega_o,X_n),\quad (n=1,2,\ldots,Z). \tag{108}$$

Summing up Eqs. (105)–(108), the total force is defined as

$$f_{TKQ}(t)=f_m+\chi_{KL}\sum_{n=1}^{Z}\left|\overline{K}_e(n\omega_o,X_n)\right|\mathrm{Re}\left[e^{i[n\omega_o t+\varphi_{Xn}+\varphi_{KQ}(n\omega_o,X_n)]}\right]. \tag{109}$$

Likewise, the force is alternately estimated by using $\overline{H}_e(n\omega_o,X_n)$ as

$$f_{THQ}(t)=f_m+\sum_{n=1}^{Z}\chi_{HQ}(n\omega_o,X_n)\left|\overline{H}_e(n\omega_o,X_n)\right|\mathrm{Re}\left[e^{i[n\omega_o t+\varphi_{Pun}+\varphi_{HL}(n\omega_o,X_n)]}\right], \tag{110}$$

$$\chi_{HQ}(n\omega_o,X_n)=A_r\left|P_u(n\omega_o,X_n)\right|\quad (n=1,2,\ldots,Z). \tag{111}$$

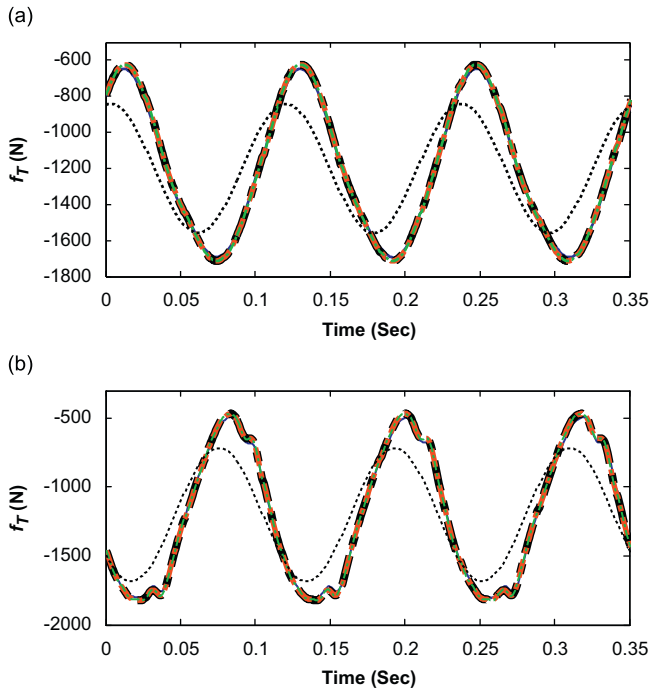

Fig. 15. Comparison of LTI and quasi-linear (QL) models with experiment in time domain, given $x(t) = \mathrm{Re}[\tilde{X}\, e^{i\omega_o t}]$ at $\omega_o/2\pi = 8.5$ Hz and $X = 1.5$ mm: (a) fixed decoupler and (b) free decoupler. Key: ——, experiment; ……, LTI (scheme I-A with ω_o term only); – –, QL scheme I-B; — ▪ , QL scheme II-C; and — ▪ , QL scheme III-C.

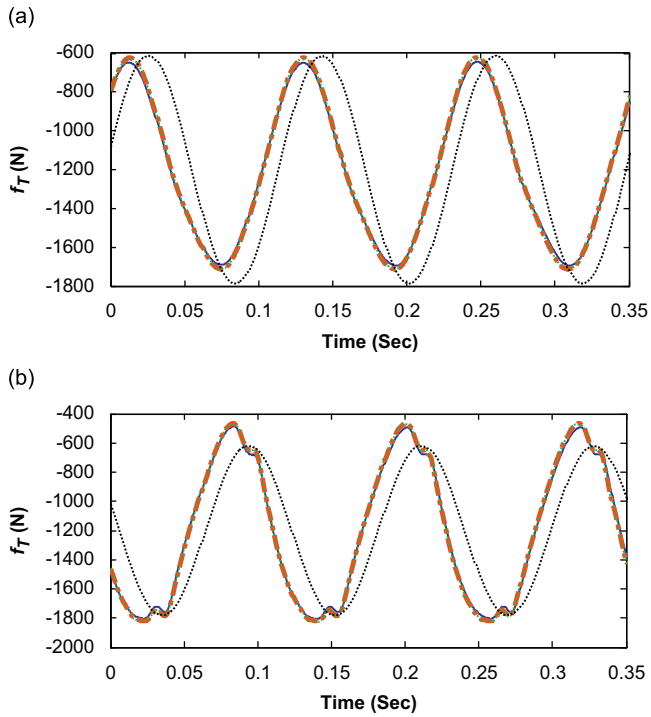

Fig. 16. Comparison of fluid and analogous mechanical system models with experiment in time domain, given $x(t) = \mathrm{Re}[\tilde{X}\, e^{i\omega_o t}]$ at $\omega_o/2\pi = 8.5$ Hz and $X = 1.5$ mm: (a) fixed decoupler and (b) free decoupler. Key: ——, experiment ; — ▪ , QL scheme II-C; ▪ ▪ ▪ , QL scheme III-C; ……, QL scheme IV-C.

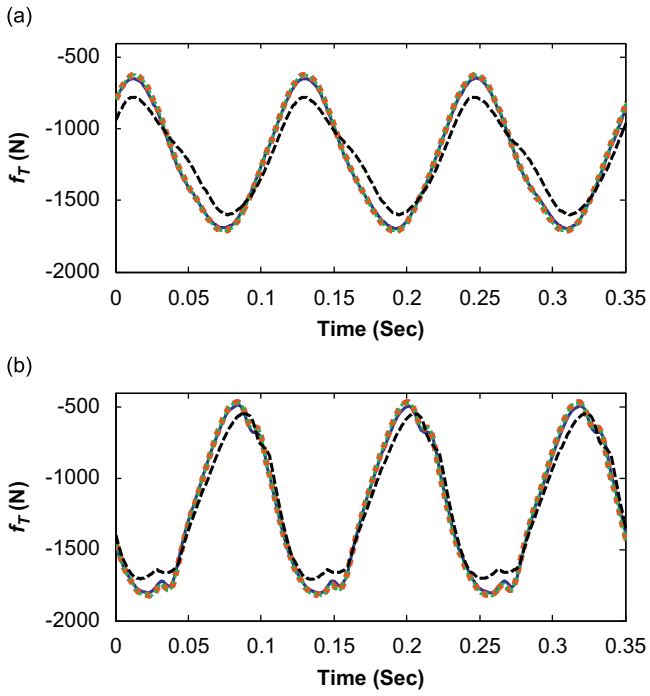

Fig. 17. Comparison of nonlinear (NL) and quasi-linear (QL) models with experiment in time domain, given $x(t) = \mathrm{Re}[\tilde{X}\, e^{i\omega_o t}]$ at $\omega_o/2\pi = 8.5$ Hz and $X = 1.5$ mm: (a) fixed decoupler and (b) free decoupler. Key: ——, experiment; — ▪ —, QL scheme II-C; ▪▪▪▪, QL scheme III-C; – –, nonlinear (NL) model.

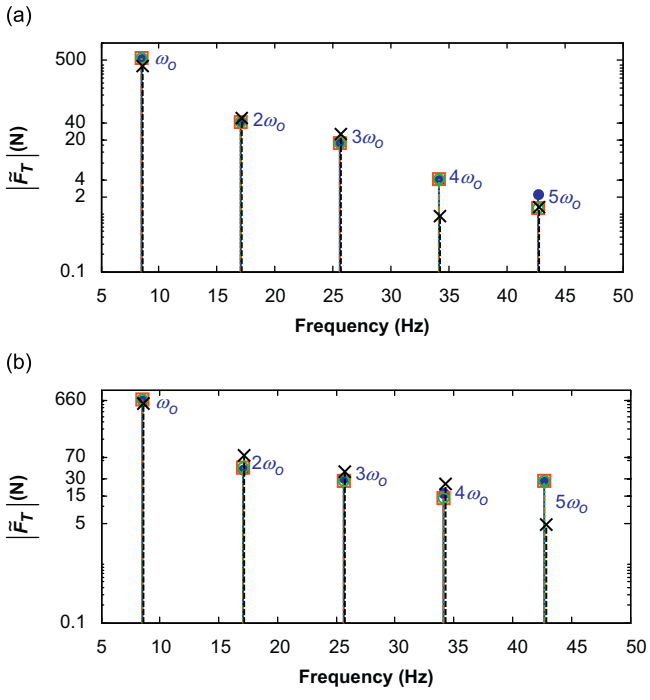

Fig. 18. Comparison of super-harmonics between nonlinear (NL) and quasi-linear (QL) models with experiment given $x(t) = \mathrm{Re}[\tilde{X}\, e^{i\omega_o t}]$ at $\omega_o/2\pi = 8.5$ Hz and $X = 1.5$ mm: (a) fixed decoupler and (b) free decoupler. Key: —●—, experiment; —□—, QL scheme II-C; —○—, QL scheme III-C; —×—, nonlinear (NL) model.

Using the same method, the analogous mechanical system model yields the following force:

$$f_{TKA}(t) = f_m + \chi_{KL} \sum_{n=1}^{Z} \left|\overline{K}_{Ae}(n\omega_o, X_n)\right| \mathrm{Re}\left[e^{in\omega_o t + \varphi_{Xn} + \varphi_{KA}(n\omega_o, X_n))}\right], \tag{112}$$

$$\varphi_{KA}(n\omega_o, X_n) = \angle \overline{K}_{Ae}(n\omega_o, X_n), \quad (n = 1,2,\ldots,Z). \tag{113}$$

Table 3
Comparison of the model estimation errors at $\omega_o/2\pi$=8.5 Hz and X=1.5 mm for alternate force estimation schemes.

Model and scheme designation		*RMS error, E (%)*	
		Fixed decoupler	*Free decoupler*
Fluid system model (Fig. 1)			
Simple prediction model given measured data	ω_o only	20.1	25.2
	with $n\omega_o$ *terms* (n=1, 2, 3, …)	6.9	11.4
Nonlinear model (NL)		11.7	10.9
Linear time-invariant model (LTI)	***I-A***	20.1	25.2
Quasi-linear model (QL)	***I-B***	1.82	2.56
	II-A	19.0	23.0
	II-B	61.9	51.0
	II-C	1.82	2.56
	III-A	19.0	23.0
	III-B	65.8	101.3
	III-C	1.82	2.60
Analogous mechanical system model (Fig. 3)			
Linear time-invariant model (LTI)	***IV-A***	23.6	38.6
Quasi-linear model (QL)	***IV-B***	23.0	27.3

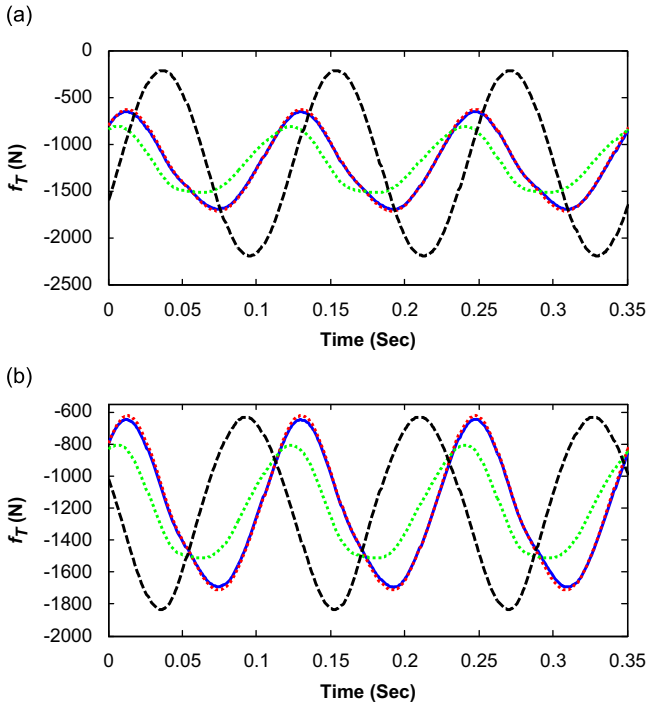

Fig. 19. Comparison of alternate quasi-linear (QL) models in time domain for the fixed decoupler mount, given $x(t) = \mathrm{Re}[\tilde{X}\, e^{i\omega_o t}]$ at $\omega_o/2\pi$=8.5 Hz and X=1.5 mm: (a) dynamic stiffness ($\tilde{K}_e$) concept and (b) force transmissibility ($\tilde{H}_e$) concept. Key: ——, experiment; — ·, QL schemes II-C and III-C; ····, QL schemes II-A and III-A; – –, QL schemes II-B and III-B.

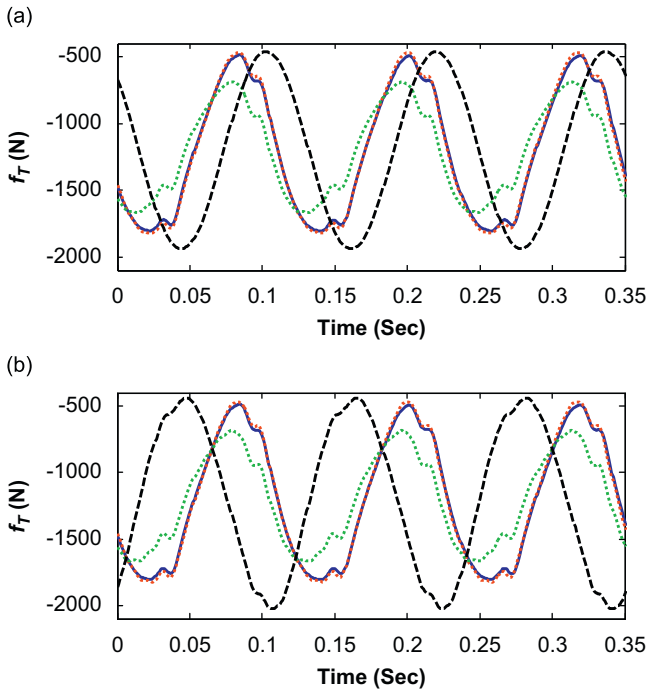

Fig. 20. Comparison of alternate quasi-linear (QL) models in time domain for the free decoupler mount, given sinusoidal displacement $x(t) = \mathrm{Re}[\tilde{X}\, e^{i\omega_o t}]$ at $\omega_o/2\pi$=8.5 Hz and X=1.5 mm: (a) dynamic stiffness ($\tilde{K}_e$) concept and (b) force transmissibility ($\tilde{H}_e$) concept. Key: ——, experiment ; — ▪ —, QL schemes II-C and III-C; ▪▪▪▪, QL schemes II-A and III-A; – –, QL schemes II-B and III-B.

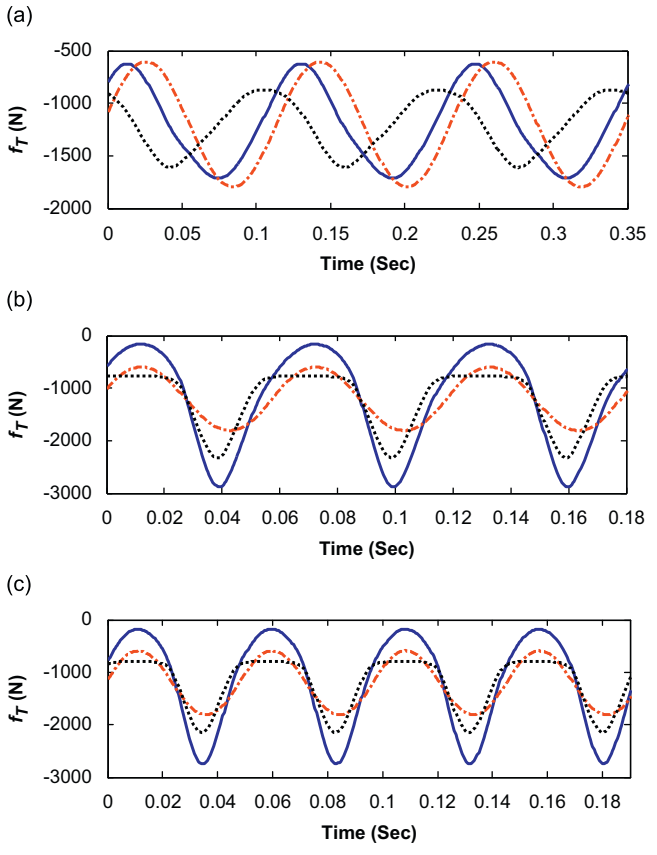

Fig. 21. Comparison between rubber and hydraulic path forces in time domain for the fixed decoupler mount given sinusoidal displacement $x(t) = \mathrm{Re}[\tilde{X}\, e^{i\omega_o t}]$ at X=1.5 mm: (a) $\omega_o/2\pi$=8.5 Hz; (b) $\omega_o/2\pi$=16.5 Hz; (c) $\omega_o/2\pi$=20.5 Hz. Key: ——, total force $f_{TH}(t)$; — ▪ —, rubber path force $f_{THr}(t)$; ……, hydraulic path force $f_{THh}(t)$.

9. Results and discussion

9.1. Comparison of models

Our study includes 12 harmonic terms in the quasi-linear (QL) models. Fig. 15 compares three QL schemes. Here, the LTI (or the simple prediction) model employs measured $x_M(t)$ and $p_{uM}(t)$ with ω_o term only. The QL schemes are based upon Eqs. (1)–(3) and (104)–(111), and are designated by I-B, II-C and III-C. The forces estimated by the QL schemes match well with measured force time histories. Conversely, the mechanical model, with QL scheme IV-C, fails to predict $f_T(t)$ as seen in Fig. 16. This is due to the $\overline{K}_{Ae}$ formulation based upon the system of Fig. 3. In particular, the numerator of $\overline{K}_{Ae}$ does not include any system properties unlike the fluid model. Also, the mechanical system does not properly incorporate the dynamic compliance $\tilde{C}_{ue}(n\omega_o, X_n)$ in the $f_T(t)$ expression as observed in Fig. 3.

Fig. 17 compares the nonlinear (NL) model with two quasi-linear models (schemes II-C and III-C). Observe the NL model shows some discrepancies in the time domain. To examine the underlying cause, spectral contents are compared in Fig. 18 for NL and QL models on a logarithmic scale. Specifically, the NL models predict lower magnitudes at $4\omega_o$ and $5\omega_o$ for both fixed and free decouplers; conversely, two QL schemes match experimental data very well.

9.2. Comparison of model errors

The normalized error $\varepsilon(t)$ between measured force $f_{TM}(t)$ and predicted force $f_T(t)$ at any time t is calculated as $\varepsilon(t) = (f_T(t) - f_{TM}(t))/f_{TM}(t)$. The overall root-mean-square (RMS in %) error E is then given by $E = 100\sqrt{(1/N_{\max})\sum_{\nu=1}^{N_{\max}}[\varepsilon(t_\nu)]^2}$, where $N_{\max}$ is the maximum number of points in time domain. Table 3 lists E values for all models in Table 2. Errors from the QL schemes such as I-B, II-C and III-C are much lower than other models. In particular, the nonlinear model shows more than 10% error even though it includes four nonlinear expressions. The chief reason is that the nonlinear profiles were measured under the static conditions as thus they do not fully capture the dynamic forces under the sinusoidal excitation conditions.

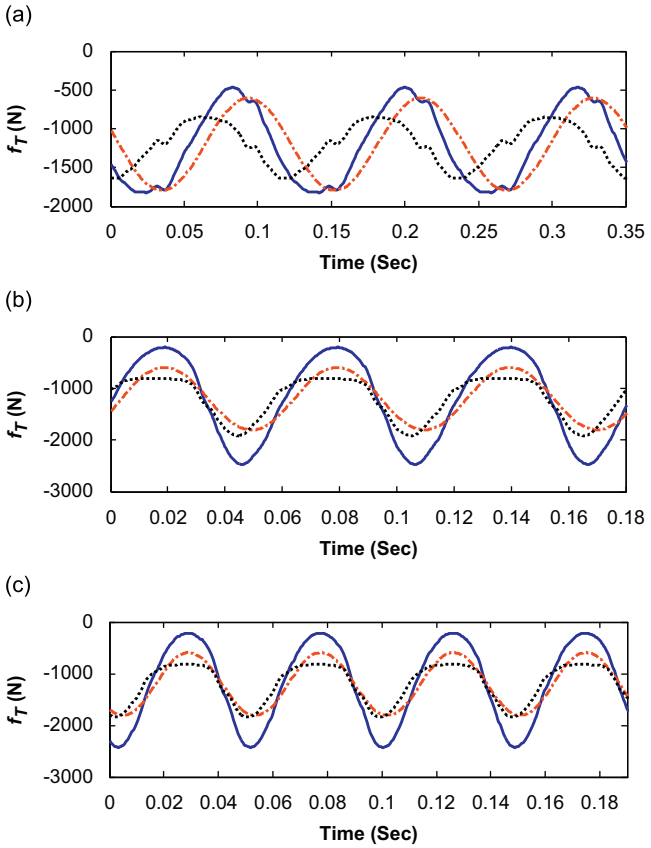

Fig. 22. Comparison between rubber and hydraulic path forces in time domain for the free decoupler mount given sinusoidal displacement $x(t) = \mathrm{Re}[\tilde{X}\, e^{i\omega_o t}]$ at X=1.5 mm: (a) $\omega_o/2\pi$=8.5 Hz; (b) $\omega_o/2\pi$=16.5 Hz; (c) $\omega_o/2\pi$=20.5 Hz. Key: ——, total force $f_{TH}(t)$; — ▪ —, rubber path force $f_{THr}(t)$; ·····, hydraulic path force $f_{THh}(t)$.

9.3. Comparison of rubber and hydraulic paths

Figs. 19 and 20 compare the quasi-linear models with a combination of $\lambda_{kr}(\omega_o,X_1)$, $\lambda_{cr}(\omega_o,X_1)$, and $\tilde{\lambda}_u(n\omega_o,X_n)$. The results reveal significant discrepancies from the measured force time history. This suggests that $\tilde{\lambda}_u(n\omega_o,X_n)$ is the most important parameter though all must be retained.

Figs. 21 and 22 compare the rubber path force $f_{THr}(t)$ and the hydraulic path force $f_{THh}(t)$ based upon the QL scheme III-C at three excitation frequencies with X=1.5 mm. The peak-to-peak value of $f_{THh}(t)$ is less than $f_{THr}(t)$ below 10 Hz. The $f_{THh}(t)$ is larger than $f_{THr}(t)$ for the fixed decoupler mount between 10 and 20 Hz. Beyond 20 Hz, $f_{THr}(t)$ and $f_{THh}(t)$ are almost the same in terms of peak-to-peak values. However, $f_{THr}(t)$ remains almost sinusoidal at all frequencies, but $f_{THh}(t)$ consists of multi-harmonic terms as observed in Figs. 21 and 22. Further, the rubber path forces $f_{THr}(t)$ are similar in fixed and free decoupler mounts, but, the contribution of hydraulic path force $f_{THh}(t)$ is smaller in the free decoupler mount when compared with the fixed decoupler mount. This is primarily due to the dynamic fluid flow through the decoupler element.

10. Conclusion

This article has proposed new methods to estimate dynamic forces (in both time and frequency domains) that are transmitted by a hydraulic mount under sinusoidal excitation. The super-harmonic contents of measured upper chamber pressure $p_{uM}(t)$ and force $f_{TM}(t)$ are examined and correlated. Effective parameters $k_{re}(\omega_o,X_1)$, $c_{re}(\omega_o,X_1)$ and $\tilde{C}_{ue}(n\omega_o,X_n)$ at the fundamental frequency and super-harmonics ($n\omega_o$) are quantified for rubber and hydraulic force paths. This leads to the development of an improved quasi-linear model with spectrally varying and amplitude-sensitive parameters. The rubber force path is considered only at ω_o, but the hydraulic path compliance $\tilde{C}_{ue}(n\omega_o,X_n)$ is quantified at $n\omega_o$ terms. Alternate relevant transfer function formulations with $n\omega_o$ terms are also examined by employing the Fourier series expansion as well as the reverse path spectral method. The causality problem should be carefully considered before employing such formulations in time domain based on frequency domain measurements [21–23]. Finally, the hydraulic mount also exhibits a sub-harmonic term response [15]. This period-doubling effect and a more refined nonlinear model should be the subject of future research. We are also incorporating the load sensing device in a real system consisting of a vehicle powertrain and its sub-frame. Overall, the methods of this paper can be extended to real-life systems where in-situ dynamic forces must be assessed.

Acknowledgements

We are grateful to the member organizations of the Smart Vehicle Concepts Center (www.SmartVehicleCenter.org) and the National Science Foundation Industry/University Cooperative Research Centers program (www.nsf.gov/eng/iip/iucrc) for supporting this work.

References

[1] A. Gunduz, A. Inoue, R. Singh, Estimation of interfacial forces in time domain for linear system, *Journal of Sound and Vibration* 329 (2010) 2616–2634.
[2] J.Y. Yoon, R. Singh, Dynamic force transmitted by hydraulic mount: estimation in frequency domain using motion and/or pressure measurements and quasi-linear models, *Noise Control Engineering Journal* 58 (4) (2010).
[3] Q. Leclere, C. Pezerat, B. Laulagnet, L. Polac, Indirect measurement of main bearing loads in an operating diesel engine, *Journal of Sound and Vibration* 286 (2005) 341–361.
[4] S.H. Yap, B.M. Gibbs, Structure-borne sound transmission from machines in buildings, part 1: indirect measurement of force at the machine–receiver interface of a single and multi-point connected system by a reciprocal method, *Journal of Sound and Vibration* 222 (1) (1999) 99–113.
[5] A. Inoue, S. Kim, R. Singh, Comparative evaluation of structure-borne noise transfer paths in a laboratory experiment, *Noise Control Engineering Journal* 54 (6) (2006) 382–395.
[6] A. Inoue, R. Singh, G.A. Fernandes, Absolute and relative path measures in a discrete system by using two analytical methods, *Journal of Sound and Vibration* 313 (2008) 696–722.
[7] MTS Elastomer Test System 831.50, 1000 Hz model, 〈http://www.mts.com〉.
[8] J.Y. Park, R. Singh, Effect of non-proportional damping on the torque roll axis decoupling of an engine mounting system, *Journal of Sound and Vibration* 313 (2008) 841–857.
[9] Acoustics and vibration-Laboratory measurement of vibro-acoustic transfer properties of resilient elements, ISO 10846: 1997 (International Organization for Standardization, Geneva, Switzerland, 1997).
[10] R. Singh, G. Kim, P.V. Ravindra, Linear analysis of automotive hydro-mechanical mount with emphasis on decoupler characteristics, *Journal of Sound and Vibration* 158 (2) (1992) 219–243.
[11] R. Singh, Rubber and hydraulic mounts: dynamic analysis, experimental characterization and vehicle vibration isolation, Course notes for the General Motors Technical Education Program, 2004.
[12] S. He, R. Singh, Estimation of amplitude and frequency dependent parameters of hydraulic engine mount given limited dynamic stiffness measurements, *Noise Control Engineering Journal* 53 (6) (2005) 271–285.
[13] G. Kim, R. Singh, Nonlinear analysis of automotive hydraulic engine mount, *ASME Journal of Dynamic Systems, Measurement and Control* 115 (3) (1993) 482–487.
[14] G. Kim, R. Singh, A study of passive and adaptive hydraulic engine mount systems with emphasis on non-linear characteristics, *Journal of Sound and Vibration* 179 (3) (1995) 427–453.
[15] M. Tiwari, H. Adiguna, R. Singh, Experimental characterization of a nonlinear hydraulic engine mount, *Noise Control Engineering Journal* 51 (1) (2003) 36–49.

[16] H. Adiguna, M. Tiwari, R. Singh, H.E. Tseng, D. Hrovat, Transient response of a hydraulic engine mount, *Journal of Sound and Vibration* 268 (2003) 217–248.
[17] R.A. Ibrahim, Recent advances in nonlinear passive vibration isolators, *Journal of Sound and Vibration* 314 (2008) 371–452.
[18] S. He, R. Singh, Discontinuous compliance nonlinearities in the hydraulic engine mount, *Journal of Sound and Vibration* 307 (2007) 545–563.
[19] J.H. Lee, R. Singh, Nonlinear frequency responses of quarter vehicle models with amplitude-sensitive engine mounts, *Journal of Sound and Vibration* 313 (2003) 784–805.
[20] J.H. Lee, R. Singh, Existence of super-harmonics in quarter-vehicle system responses with nonlinear inertia hydraulic track mount given sinusoidal force excitation, *Journal of Sound and Vibration* 313 (2008) 367–374.
[21] A. Papoulis, in: *The Fourier Integral and Its Applications*, McGraw-Hill, New York, 1962.
[22] J.H Lee, K.J. Kim, Treatment of frequency-dependent complex stiffness for commercial multi-body dynamic analysis programs, *Mechanics of Structures and Machines* 30 (4) (2002) 527–541.
[23] J.S. Bendat, A.G. Piersol, in: *Random Data: Analysis and Measurement Procedures*, John Wiley & Sons, New York, 2000.
[24] T.C. Kim, T.E. Rook, R. Singh, Effect of smoothening functions on the frequency response of and oscillator with clearance non-linearity, *Journal of Sound and Vibration* 263 (3) (2003) 665–678.
[25] C.M. Richards, R. Singh, Identification of multi-degree-of-freedom non-linear systems under random excitations by the ''reverse path'' spectral method, *Journal of Sound and Vibration* 213 (4) (1998) 673–708.
[26] J.S. Bendat, in: *Nonlinear System Analysis and Identification from Random Data*, Wiley-Interscience, New York, 1990.